The Astrophysical Journal, 969:63 (20pp), 2024 July 1 https://doi.org/10.3847/1538-4357/ad47b6
© 2024. The Author(s). Published by the American Astronomical Society.
OPEN ACCESS

Binding Energies of N-bearing Species on Interstellar Water Ice Mantles by Quantum Chemical Calculations

Berta Martínez-Bachs[1], Stefano Ferrero[1], Cecilia Ceccarelli[2], Piero Ugliengo[3], and Albert Rimola[1]
[1] Departament de Química, Universitat Autònoma de Barcelona, Bellaterra, 08193, Catalonia, Spain; albert.rimola@uab.cat
[2] Univ. Grenoble Alpes, CNRS, Institut de Planétologie et d'Astrophysique de Grenoble (IPAG), 38000 Grenoble, France
[3] Dipartimento di Chimica and Nanostructured Interfaces and Surfaces (NIS) Centre, Università degli Studi di Torino, via P. Giuria 7, 10125, Torino, Italy
Received 2024 February 14; revised 2024 April 10; accepted 2024 May 3; published 2024 July 1

Abstract

Of the about 300 gas-phase molecular species so far detected in the interstellar medium (ISM), mostly via observations of their rotational lines, around 40% contain nitrogen (N) atoms. Likewise, of the less than a dozen interstellar molecules, firmly or likely detected in the solid-state water-dominated icy matrix by means of infrared observations, two bear N. A crucial parameter that regulates whether a species is in the gas or adsorbed on the icy phase is their binding energy (BE) toward the icy grain. Therefore, an accurate quantification of the BE is of paramount importance to properly model the ISM chemistry through numerical models. However, very few BEs are available in the literature, either determined experimentally or theoretically. In the present study, we calculate the BEs of 21 among the most abundant interstellar N-bearing species. We adopted two structural water ice models, representing a crystalline and an amorphous surface, using a reliable cost-effective procedure based on the density functional theory. While on the crystalline surface model only one BE per species is obtained due to the high symmetry of the unit cell, on the amorphous model from 5 to 10 BEs are obtained, due to its richer surface morphological variety. Most of our computed BEs agree with available experimental and other computational values. Finally, we discuss how the newly computed BEs can help estimate which N-bearing species can be frozen at the water snow line and, therefore, incorporated in water-rich ice planetesimals.

Unified Astronomy Thesaurus concepts: Surface ices (2117); Interstellar dust (836); Interstellar molecules (849); Dense interstellar clouds (371); Interstellar medium (847); Solid matter physics (2090); Interstellar dust processes (838); Computational methods (1965)

1. Introduction

The interest to understand the chemical evolution of the interstellar medium (ISM) started more than 80 yr ago, when the first diatomic species CH, CN, and CH^+ were detected (Dunham 1937; Swings & Rosenfeld 1937; McKellar 1940; Douglas & Herzberg 1941). Currently, more than 290 gas-phase species have been detected in the ISM through their rotational and vibrational transitions (McGuire 2022; Endres et al. 2016). Of these, about 40% contain N-bearing atoms, making this class of interstellar detected molecules the fourth most numerous, after H-, C-, and O-bearing species. Obviously, this is a consequence of the relative nitrogen abundance in the ISM (the fifth after H, He, O, and C) and its chemical propensity to combine with other atoms. In addition, nitrogen is a key element for life, in which N-bearing compounds played a crucial role in chemical processes that could have eventually led to the emergence of life (e.g., synthesis of amino acids and nucleotides; Saladino et al. 2012a; Saitta & Saija 2014; Santalucia et al. 2022).

In molecular clouds, the cold and dense regions of the ISM, the gas (consisting of atoms and molecules) is mixed with solid-state dust grains. The latter have cores of either silicates or carbonaceous materials, which are covered by thick ice mantles, made predominantly of water (formed in situ), but also of other volatile species such as CO, CO_2, NH_3, CH_3OH, and CH_4. For this reason, these ices are commonly referred to as "dirty ices" (Boogert et al. 2015). Regarding N-bearing species, in addition to ammonia, the likely detection of solid OCN^- and NH_4^+ has also been reported (e.g., McClure et al. 2023).

Observational measurements based on infrared spectroscopy reveal that interstellar ices are likely to be in an amorphous state (Watanabe & Kouchi 2008; Oba et al. 2009; Boogert et al. 2015; McClure et al. 2023). The composition of the ices is the result of the adsorption of species coming from the external gas environment as well as of chemical reactions occurring on their surfaces. Thus, the binding energy (BE) of each species to the icy dust mantle and the dust temperature are the most important parameters that regulate whether the species is in the gas or solid phase.

Observational measurements are usually interpreted via astrochemical numerical models, which aim to reproduce and understand the chemical behavior of the ISM. In these models, various parameters need to be introduced as input data, those describing the physical status of the object to model and others describing the chemical processes (e.g., Ceccarelli 2023). BEs are crucial parameters, since they are directly associated with the ice-to-gas transition in desorption events. Additionally, other surface processes also depend on the BEs of adsorbed species like the diffusion, in which diffusion barriers are commonly assumed to be a fraction of its BE (Cuppen et al. 2017; Penteado et al. 2017). Therefore, having accurate BE values of interstellar species is of uttermost importance for the reliability of the astrochemical modeling outcomes and, hence, to properly know and understand the chemical evolution and composition of the ISM.

Experimentally, BEs are determined by means of temperature-programmed desorption (TPD) experiments. They

Original content from this work may be used under the terms of the Creative Commons Attribution 4.0 licence. Any further distribution of this work must maintain attribution to the author(s) and the title of the work, journal citation and DOI.

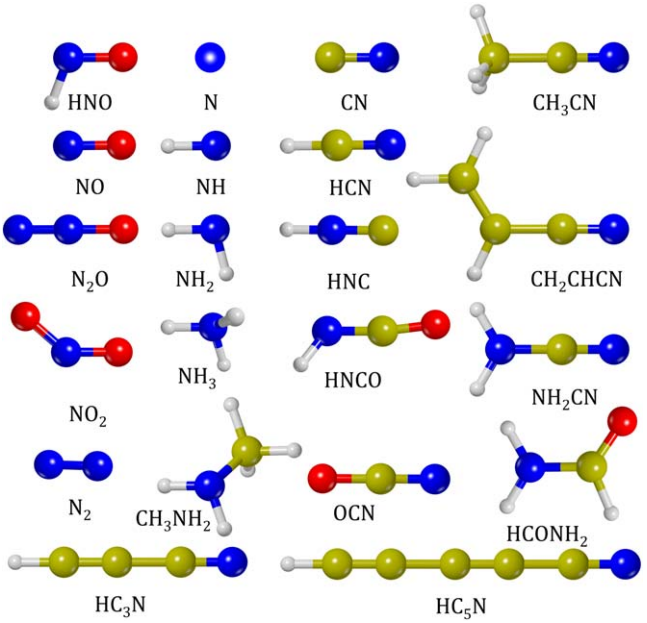

Figure 1. Set of N-bearing species considered in this work. Green represents carbon atoms, blue nitrogen, red oxygen, and gray hydrogen.

basically consist of three consecutive steps: (i) the substrate is carefully prepared by condensing water in a phase as close as possible to that observed in the ISM icy grains; (ii) the substrate is exposed to the adsorption of the species at a (very low) constant temperature, and (iii) the temperature below the substrate is increased through a defined ramp in time to measure the desorption rate of the species as a function of the temperature, usually detected with mass spectrometry (Noble et al. 2012; Penteado et al. 2017). Then, by a proper mathematical manipulation of the Polanyi–Wigner equation (Kolasinski 2012), which describes the desorption process, the BE and the desorption rate preexponential factor are worked out from the experimental TPD data. There is no unique way to derive the BE and the preexponential factor from the experiments, causing some degree of variability in these data and difficulties in making proper comparisons. To be noticed, TPD experiments do not measure the BEs of the species but its desorption enthalpy, which is usually equivalent to the BE, if no other activated processes take place (He et al. 2016). In general, BE values obtained through TPD experiments are strongly affected not only by the composition and morphology of the icy surface but also by the adsorbate coverage. Despite the great amount of work done investigating desorption processes via TPD experiments, BEs on amorphous water ices have been derived only for less than two dozen molecules (e.g., Dohnálek et al. 2001; Collings et al. 2004; Noble et al. 2012; Dulieu et al. 2013; Fayolle et al. 2016; He et al. 2016; Smith et al. 2016; Chaabouni et al. 2018; Ferrero et al. 2022; Minissale et al. 2022). In addition, TPD experiments cannot deal with radical species due to their high reactivity (Cuppen et al. 2017; Minissale et al. 2022).

BEs can also be obtained theoretically by means of quantum chemical calculations. In this way, many TPD limitations can be overcome, like dealing with open-shell species (e.g., radicals). Several computational studies have derived the BEs of species such as H, H_2, C, N, O, OH, CO, CO_2, HCO, H_2O, NH_3, and HF on periodic/cluster crystalline/amorphous model systems of different sizes (e.g., Al-Halabi & Van Dishoeck 2007; Karssemeijer & Cuppen 2014; Karssemeijer et al. 2014; Ásgeirsson et al. 2017; Sameera et al. 2017; Senevirathne et al. 2017; Zamirri et al. 2017, 2019; Shimonishi et al. 2018; Bovolenta et al. 2020; Duflot et al. 2021; Germain et al. 2022; Tinacci et al. 2022, 2023; Hendrix et al. 2023). Other computational studies calculated the BEs of a large number of interstellar species, but adopting as a substrate very small ice models. For instance, in Wakelam et al. (2017), it was assumed a single water molecule is representative of the whole grain, despite some clever a posteriori corrections to overcome such a limitation. A different strategy was carried out by Das et al. (2018) and Hendrix et al. (2023), in which water ice surfaces were mimicked by clusters made up by up to four/six water molecules. However, none of these two surface approaches can fairly reproduce the amorphous nature of water icy dust grains. Moreover, these models are not large enough to ensure the occurrence of H-bond cooperativity, which affect the binding capacity of the surface adsorption sites. In contrast, Duflot et al. (2021) performed BE calculations by combining force field molecular dynamics (MD) simulations with quantum chemical calculations on some configurations emerged from the MD sampling for a set of atoms and molecules on hexagonal ice and amorphous cluster models. The use of the ONIOM procedure (by combining density functional theory, hereafter DFT, with semiempirical methods for the description of the binding site and environmental regions, respectively) allowed the authors to use cluster models of 120–150 atoms, this way overcoming the cluster size and the lack of H-bonding cooperativity limitations mentioned above.

In a recent work, Ferrero et al. (2020) computed a large set of BEs for 21 astrochemical-relevant species, both on a crystalline and on amorphous periodic water ice surface models. Both models properly reproduce the behavior of interstellar water ices and ensure the cooperativity of hydrogen-bonded interacting systems. For the crystalline model, since only a few possible adsorption sites exist, just one or two BEs were computed for each species. In contrast, on the amorphous water ice model, a broad distribution of BEs for each species was calculated because multiple adsorption sites were considered. In a more recent work, Perrero et al. (2022) followed a methodology similar to that of Ferrero et al. (2020) to compute the BE distributions of 17 S-bearing species absorbed on the same crystalline and amorphous periodic water ice models.

The present work adopts the same approach, i.e., ice models and methodology of Ferrero et al. (2020) and Perrero et al. (2022), to study the adsorption features of a set of 21 N-bearing species (summarized in Figure 1). The 21 chosen N-bearing species include 14 closed-shell species (NH_3, HCN, HNC, N_2, HNO, CH_3NH_2, CH_3CN, NH_2CN, HNCO, N_2O, NH_2CHO, HC_3N, CH_2CHCN, and HC_5N) and seven open-shell species (N, NH, NH_2, CN, NO, OCN, and NO_2). Six species (NH_3, HCN, N_2, CH_3CN, NH_2CHO, and NH_2) were already present in the Ferrero et al. (2020) work, and we repeated the computations of their BEs to ensure internal consistency, as the method applied here may slightly differ in some aspects (see Section 2). Moreover, for each species, the desorption rate preexponential factors were computed, as they are crucial to work out the BEs from the TPD experiments.

All the studied species have been detected in the ISM with one exception, NO_2. In particular, the sample consists of detected neutral N-bearing species not containing atoms

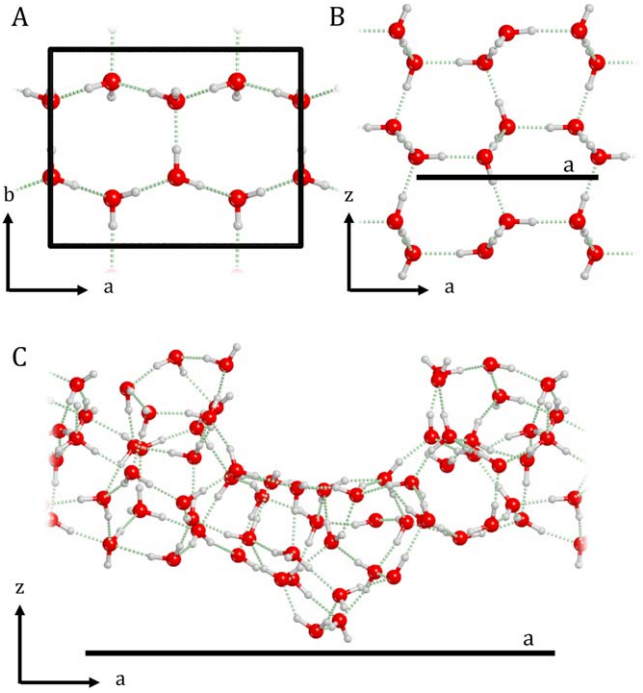

Figure 2. Top view (A) and lateral view (B) of the crystalline water surface model; (C) side view of the amorphous solid water surface. The black lines indicate the unit cell sizes.

that belong to the third period (e.g., NS—computed in Perrero et al. 2022, PN and SiN, etc.). With this rule, all the di-atomic and tri-atomic N-species, with one exception (C_2N), are considered in the present study, whereas we included half of the neutral N-bearing species with four atoms and a smaller fraction with a larger number of atoms. Generally speaking, we privileged the polyatomic species, which are more often detected in star-forming regions, which in turn also implies having the largest abundances.

The goal of the present study is to provide the community with accurate BE values and distributions of these species on water-rich ices so that they can serve as useful input data in astrochemical models, as well as the corresponding desorption rate preexponential factors. As already mentioned, the correct modeling of the species desorption is a basic need for rationalizing the observations to ultimately understand the ISM chemistry.

2. Methodology

2.1. Water Ice Surface Models

The surfaces mimicking the interstellar water ice mantles were modeled adopting a periodic approach. In particular, two model systems were adopted: a crystalline system and an amorphous system.

As a first approach, a crystalline water ice surface model based on the P-ice structure was used for the adsorption of the N-bearing compounds. P-ice is the proton-ordered analog to the hexagonal (proton-disordered) water ice, which has been demonstrated to reproduce fairly well the physicochemical features of crystalline water ice (Pisani et al. 1996). The surface model was generated by cutting out the P-ice 3D periodic bulk structure perpendicular to the [010] direction, resulting in the (010) slab surface model. This choice is because the (010) slab model is one of the most stable planes of the crystalline P-ice, and it has no dipole component across the surface (Casassa et al. 1997; Zamirri et al. 2018). The use of P-ice offers an advantage due to its small unit cell, which efficiently treats the adsorption of small species on its surfaces. Furthermore, when dealing with molecules of large size, it is easy and computationally efficient to adopt the supercell strategy, as explained in the following paragraph. A non-proton-ordered model of I_h ice would be, for the present purposes, too expensive computationally, as the unit cell should be large enough to represent enough local environment of each water molecules. For a crystalline ice, it is important that the long-range H-bonding cooperativity is taken into account while ensuring zero dipole moment across the considered slab models, both features exhibited by the P-ice model. This crystalline water surface (CWS) model consists of 12 atomic layers, with a whole thickness of 10.9 Å, and includes 24 water molecules (72 atoms) per unit cell (see Figures 2(A) and (B)). The cell parameters are $|a| = 9.066$ Å and $|b| = 7.155$ Å, resulting in a surface area of $A = 64.863$ Å^2. For this CWS model, to simulate the adsorption of the large HC_3N and CH_2CHCN species, we adopted a 1×2 unit cell (namely, the b lattice parameter was doubled) giving rise to a surface that contains 48 water molecules (144 atoms) to avoid lateral interactions between unit cell replicas. For this 1×2 surface model, the cell parameters are $|a| = 9.066$ Å and $|b| = 14.310$ Å, resulting in a surface area of $A = 129.726$ Å^2. Certainly, the CWS model does not represent the structural features of interstellar water ices since they are mostly in an amorphous form (Watanabe & Kouchi 2008; Boogert et al. 2015). However, this model has been very useful to assess the accuracy of the employed methodology due to the cheaper cost of the calculations compared to the amorphous model (see below).

With the aim to obtain BE values on more realistic interstellar surfaces, an amorphous solid water (ASW) surface model, first proposed by Ferrero et al. (2020), was adopted. It is a slab model based on a periodic approach, which was constructed by joining small water clusters obtained from Shimonishi et al. (2018). In this case, a large unit cell was considered (cell parameters of $|a| = 20.352$ Å and $|b| = 10.027$ Å, and a surface area of $A = 204.071$ Å^2), consisting of 60 water molecules (180 atoms) per unit cell, in order to cover the heterogeneity of surface sites present in ASW systems. Additionally, the model presents different structural features for the upper and the lower surfaces, and therefore, different binding sites for adsorbates can be considered (see Figure 2(C)).

2.2. Computational Details

The periodic ab initio CRYSTAL17 code (Dovesi et al. 2018) was employed to carry out all the simulations. This software implements both the Hartree–Fock (HF) and the Kohn–Sham self-consistent field (SCF) methods to solve the electronic Schrödinger equation. CRYSTAL17 can simulate periodic (crystals, surfaces, and polymers) and nonperiodic (molecules) systems since it uses localized Gaussian functions as basis sets. As a result, surfaces can be defined as true slab models, hence avoiding the 3D replica usually implemented in plane waves' basis set codes.

The adsorption of the N-bearing species on the water ice models was computed adopting quantum chemical electronic structure methods. A DFT//HF-3c composite procedure was adopted to simulate the interaction between the adsorbates and the water ice slab models. In this cost-effective procedure, geometries were optimized with the HF-3c method while the

energetics were refined by performing single point calculations at the DFT level on the HF-3c optimized structures.

HF-3c is a semiempirical method in which the electronic energy is based on the HF method using a minimal Gaussian atomic orbital basis set, MINIX, in which three corrections are considered to alleviate the deficiencies caused by the approximations, namely, (i) to include dispersive interactions; (ii) to remove the basis set superposition error (BSSE) using the geometrical counterpoise (CP) correction; and (iii) to correct the short-ranged deficiencies due to using minimal basis sets (Jansen & Ros 1969; Liu & McLean 1973; Tatewaki & Huzinaga 1980; Sure & Grimme 2013).

The single point energy calculations at DFT were performed using two different methods: (i) for closed-shell species, the hybrid B3LYP functional, which includes a 20% of exact exchange, (Lee et al. 1988; Becke 1993), complemented by the D3 Grimme's empirical corrections with the Becke–Johnson (BJ) damping scheme, i.e., D3(BJ), to account for the dispersive forces (Grimme et al. 2011); and (ii) for open-shell species (atoms and radicals), the meta-hybrid M06-2X functional, which includes a 45% of exact exchange, in these cases adopting a spin-unrestricted formalism (Pople et al. 1995). For both DFT functionals, the Ahlrichs triple-zeta valence basis set with polarization functions was employed (Schäfer et al. 1992).

In order to assess the performance of the cost-effective DFT//HF-3c methodology, adsorptions were first simulated on the CWS model in a full DFT treatment (namely, geometry optimizations also at DFT, hereafter referred to as DFT//DFT). The same DFT functionals and basis set used in the DFT//HF-3c methodology were adopted in this DFT//DFT procedure.

Additionally, to ensure the accuracy of the DFT//HF-3c scheme (as well as the DFT//DFT one), an energy refinement adopting an ONIOM approach was carried out on the CWS systems, in line with other literature works citesameera2017oniom, duflot2021theoretical. In this ONIOM approach (inspired from the ONIOM2 strategy; Dapprich et al. 1999), the system is divided in two parts: (i) the model system, which here is a molecular system extracted from the crystalline periodic system that includes the adsorbate and the nearest water molecules (two or three) defining the binding site region; (ii) the real system, which is the whole system, treated as a periodic system. The two parts are computed at different theory levels: the model system at CCSD(T) as a high theory level, and the real system at DFT as a low theory level. This ONIOM approach is hereafter referred to as O[CCSD(T)//DFT]. The selection of these two regions is based on the localized nature of the interaction between the adsorbates and the binding site region. Calculations at the high and low theory levels were performed as single point energy calculations on the CWS DFT-optimized adsorption complex structures. The single point CCSD(T) energy calculations were performed with the Gaussian16 program (Frisch et al. 2016). Since the CCSD(T) method is strongly dependent on the basis set (Cramer & Bickelhaupt 2003), the Dunning correlation consistent family of basis sets (cc-pVnZ) was used to perform the calculations (Dunning 1989). Here, the Jun-cc-pVnZ family of basis set was employed, with n standing for double ("D"), triple ("T"), and quadruple ("Q"; Papajak et al. 2011), followed by extrapolation to the complete basis set by plotting the energy against $1/n^3$.

Periodic geometry optimizations were carried out by relaxing both the internal atomic positions and the cell parameters. All the adsorption complexes were characterized by calculating their harmonic frequencies, which in CRYSTAL is done numerically at the Γ point by diagonalizing the mass-weighted Hessian matrix of the second-order energy derivatives with respect to atom displacements (central difference formula), in this case of ± 0.003 Å from the minimum along each Cartesian coordinate (Pascale et al. 2004; Zicovich-Wilson et al. 2004). For the HF-3c-optimized structures, the whole periodic systems were considered in the harmonic frequency calculations. For geometries optimized at DFT, only the fragment regarding the binding region was considered (the same model system adopted in the ONIOM approach).

2.3. Calculation of the BEs

BEs were calculated from the interaction between the slab surface models and the adsorbed species. Interaction energies were calculated by considering the deformation of the surface and the adsorbates, and also the lateral interactions between adsorbates of adjacent unit cells. For localized basis functions as in this case, BSSE arises (Boys & Bernardi 1970), and, therefore, the CP correction was applied to the interaction energies (Davidson & Feller 1986).

BSSE-corrected interaction energies ($\Delta E^{\rm CP}$) were calculated as

$$\Delta E^{\rm CP} = \Delta E^{*} + \delta E_S + \delta E_\mu + \delta E_L - {\rm BSSE} \quad (1)$$

where ΔE^{*} stands for the deformation-free interaction energy, δE_S for the deformation energy of the slab model, δE_μ for the deformation energy of the adsorbate, δE_L for the adsorbate–adsorbate lateral interaction energy, and BSSE for the CP correction. Details on the calculation of each energetic term of Equation (1) can be found in the Appendix B.

BEs are defined as the opposite of BSSE-corrected interaction energies,

$$\mathrm{BE} = -\Delta E^{\rm CP}. \quad (2)$$

Within the O[CCSD(T)//DFT] scheme, the refined BEs ($\mathrm{BE}_{\mathrm{O[CCSD(T)//DFT]}}$) were calculated as

$$\begin{aligned}&\mathrm{BE}_{\mathrm{O[CCSD}(T)\,//\,\mathrm{DFT]}}\\ &= \mathrm{BE}_{(\mathrm{low;real})} + \mathrm{BE}_{(\mathrm{high;model})} - \mathrm{BE}_{(\mathrm{low;model})}\end{aligned} \quad (3)$$

where $\mathrm{BE}_{(\mathrm{low,real})}$ stands for the BE of the whole periodic (real) system at the low theory level (DFT), and $\mathrm{BE}_{(\mathrm{high,model})}$ and $\mathrm{BE}_{(\mathrm{low,model})}$ stand for the BEs of the molecular (model) system at the high (CCSD(T)) and low (DFT) theory levels, respectively. The BSSE correction was applied to these three BE terms computed in the O[CCSD(T)//DFT] framework.

Vibrational zero-point energy (ZPE) corrections of each structure were obtained from their harmonic frequency calculations (see above). The contribution of the ZPE to the BEs (ΔZPE) was then added to BE to obtain the final BE(0), namely,

$$\mathrm{BE}(0) = \mathrm{BE} - \mathrm{ZPE}. \quad (4)$$

Within the DFT//HF-3c scheme, harmonic frequencies (computed at HF-3c) are not expected to be accurate enough, and therefore, they were not used to consider ΔZPE, but only to verify that the optimized structures were really minima stationary points. In contrast, within the DFT//DFT scheme, the harmonic frequencies of the fragment (calculated at DFT) were employed to compute the ΔZPE terms. As this procedure was limited to the CWS model, a linear correlation between the

BE and the corresponding BE(0)s calculated at DFT//DFT allowed us to obtain a fitting scaling factor, which was then applied to the DFT//HF-3c BE values to obtain the corresponding BE(0) values for each adsorption complex.

2.4. Calculation of the Desorption Rate Preexponential Factor

As mentioned in the Introduction, in TPD experiments, the BE of a species on a given substrate is obtained by applying the Polanyi–Wigner equation (Kolasinski 2012), in which the desorption rate ($k_{\rm des}$(T)) is given by

$$k_{\rm des}(T) \simeq \nu(T)\, e^{-{\rm BE}(0)/(k_B T)} \tag{5}$$

where $\nu(T)$ is the desorption rate preexponential factor, and k_B is the Boltzmann constant. Thus, accurate determination of BE(0)s relies on an accurate estimate of the $\nu(T)$ value, which considers the influence of entropy in the desorption process.

As in previous articles (Minissale et al. 2022; Tinacci et al. 2022), to calculate ν, we here adopted the formula from Tait et al. (2005):

$$\nu(T) = \frac{k_B T}{h} q^{\ddagger}_{tr,2D} q^{\ddagger}_{\rm rot,3D} \tag{6}$$

where k_B is the Boltzmann constant, h is the Planck constant, $q^{\ddagger}_{tr,2D}$ is the 2D-translational partition function of the adsorbate, excluding the contribution from the translational motion perpendicular to the surface, and $q^{\ddagger}_{\rm rot,3D}$ represents the adsorbate rotational partitional function.

The 2D translational partition function is given by

$$q^{\ddagger}_{tr,2D} = \frac{2\pi m k_B T}{h^2} A \tag{7}$$

where m is the mass of the molecule, and A is the surface area per adsorbed molecule as computed using the unit cell parameters for the CWS and ASW cases.

The 3D rotational partition function is given by

$$q^{\ddagger}_{\rm rot,3D} = \frac{\sqrt{\pi}}{\sigma h^3} (8\pi^2 k_B T)^{\frac{3}{2}} \sqrt{I_x I_y I_z} \tag{8}$$

where I_i is the ith adsorbate principal moment of inertia, and σ is the symmetry adsorbate rotation factor.

For diatomic molecules and linear species, the rotational partition function is reduced to

$$q^{\ddagger}_{\rm rot,2D} = \frac{\sqrt{\pi}}{\sigma h^2} (8\pi^2 k_B T) \sqrt{I_y I_z}\,. \tag{9}$$

For atoms, only the translational partition function survives in the calculation of the desorption rate prefactor.

3. Results

This work presents the calculated BEs of the N-containing species shown in Figure 1, both on the CWS and ASW models. To this end, the considered species have been classified in two groups, according to their capability to establish hydrogen bonds (H-bonds): (i) those that can only act as H-bond acceptors (N, CN, N_2, NO, OCN, N_2O, and NO_2), hereafter referred to as Hb-A; and (ii) those that can act as both H-bond donors and acceptors (NH, NH_2, NH_3, HCN, HNC, HNO, CH_3NH_2, CH_3CN, NH_2CN, HNCO, NH_2CHO, HC_3N, CH_2CHCN, and HC_5N), hereafter referred to as Hb-AD. It is important to remark that, although CH_3CN, HC_3N, CH_2CHCN, and HC_5N belong to the Hb-AD group, they establish weak donor H-bonds since hydrogen atoms are bonded to carbon atoms.

Table 1
BEs (in Kelvin Units) Computed at DFT//HF-3c, DFT//DFT, and O[CCSD(T)//DFT] Levels on the CWS Model

Species	$BE_{DFT//HF-3c}$	$BE_{DFT//DFT}$	$BE_{O[CCSD(T)//DFT}$
N	1913	2225	1586
NH	4179	4643	4125
NH_2	6042	5939	5861
NH_3	7301	7373	7233
HCN	5725	5124	5642
HNC	8482	8756	8257
N_2	1455	1564	1477
NO	1369	1638	1695
HNO	4601	5150	4737
CH_3NH_2	8498	8455	8167
CH_3CN	7090	7551	7532
NH_2CN	10,413	10,312	9856
HNCO	8232[a]	8340	8150
N_2O	3092	3288	3430
NH_2CHO	9634	10,079	9638
NO_2	2199	2681	2751
HC_3N	3781	3886[b]	⋯
CH_2CHCN	5818	6199	6000

Notes.
[a] BEs have been computed using DFT//PBE procedure; see Section 3.1.1.
[b] BE has been interpolated from the correlation between binding energies at DFT//DFT level vs. DFT//HF-3c method; see Figure 4.

3.1. BEs for the Crystalline Systems

The BEs of all the N-containing species (with the exception of CN, OCN, and HC_5N) have been computed on the CWS model. Table 1 reports the computed BE values with the three different methodologies, namely, DFT//HF-3c, DFT//DFT, and O[CCSD(T)//DFT (see Section 2.2). The adsorption of the CN, OCN, and HC_5N on the CWS model has not achieved for either self-consistent energy or geometry optimization convergence problems, probably due to the subtle electronic structure (in the cases of CN and OCN radicals) or difficulties in fitting the HC_5N structure onto the relatively small unit cell of the CWS model.

3.1.1. BEs Computed at DFT//HF-3c

The adsorption on the CWS model was first studied at the DFT//HF-3c level. It is worth mentioning that HNCO is artificially described as a linear molecule by the HF-3c method. For this reason, and only for this specific molecule, we used the DFT Perdew-Burke-Ernzerhof (PBE; a gradient generalized approximated functional; Perdew et al. 1996) combined with the D3(BJ) term for the dispersion interactions, as an alternative method to accurately reproduce the structure of HNCO and its adsorption on the water ice surfaces. Accordingly, for the HNCO adsorption, the B3LYP-D3(BJ)//PBE-D3(BJ) procedure was performed. For the sake of simplicity, this alternative scheme is included in the reference group of DFT//HF-3c methodology.

As H-bond and dispersion forces are the main intermolecular interactions dictating the adsorption of the species on the water ice models, we manually guessed the initial structures of the

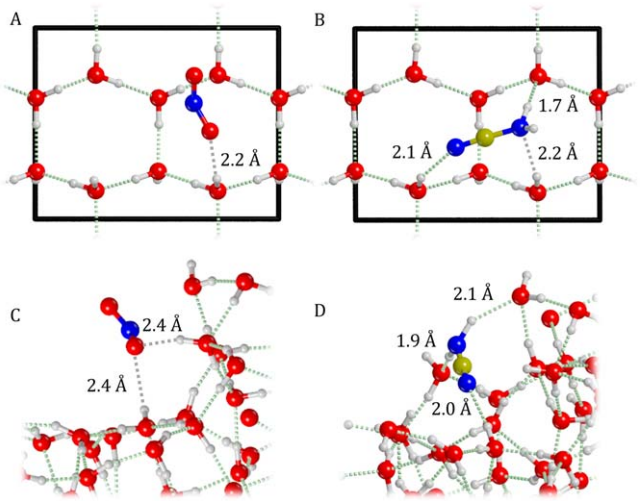

Figure 3. HF-3c optimized geometries of NO_2 and NH_2CN (as illustrative examples) on the CWS model (A and B panels) and on the ASW (case 5, C and D panels). Distances are in Angstrom.

adsorbate at the CWS model surface by maximizing the number of H-bond interactions.

As a result, $BE_{DFT//HF-3c}$ values spread in a range from 1369 to 10,413 K (see Table 1).

The general trend is that Hb-AD species present larger $BE_{DFT//HF-3c}$ values than Hb-A species (see Table 1). The $BE_{DFT//HF-3c}$ values for the Hb-AD cases span a higher range [3781–10,413 K] compared to Hb-A cases [1369–3092 K]. Hb-AD species can establish at least two H-bonds (one as H-bond donor and one as H-bond acceptor), and, even in some cases, three H-bonds. Moreover, Hb-AD group can also establish H-bonds reinforced by cooperativity. For Hb-A species, only one or, at the most, two H-bonds, are formed. Figures 3(A) and (B) report, as examples, the adsorption of NO_2 and NH_2CN (as illustrative examples of Hb-A and Hb-AD groups, respectively) on the CWS model optimized at HF-3c.

Dispersive interactions are more significant in species with larger sizes. As, in general, species belonging to Hb-AD group are larger in size than those of the Hb-A group, they give larger dispersion interactions than Hb-A species.

3.1.2. BEs Computed at DFT//DFT

To assess the performance of the cost-effective DFT//HF-3c methodology, the adsorption complexes on the CWS model have also been simulated at DFT//DFT, allowing the comparison between the $BE_{DFT//DFT}$ and the $BE_{DFT//HF-3c}$ values.

A general trend is that the $BE_{DFT//DFT}$ values are slightly higher than the $BE_{DFT//HF-3c}$, as shown in the plot of Figure 4(A). The HF-3c-optimized geometries, which are almost free from BSSE by construction, give longer H-bond distances than the DFT-optimized ones. This, in turn, gives lower-BE values for DFT//HF-3c than the DFT//DFT ones, in which the BSSE shrinks the intermolecular distances. Nevertheless, $BE_{DFT//DFT}$ well correlates with $BE_{DFT//HF-3c}$ values, as shown in Figure 4(A).

Remarkably, for HNCO, the DFT//PBE-D3(BJ) procedure is in perfect agreement with the DFT//DFT one, indicating its suitability to be used for this molecule in further calculations.

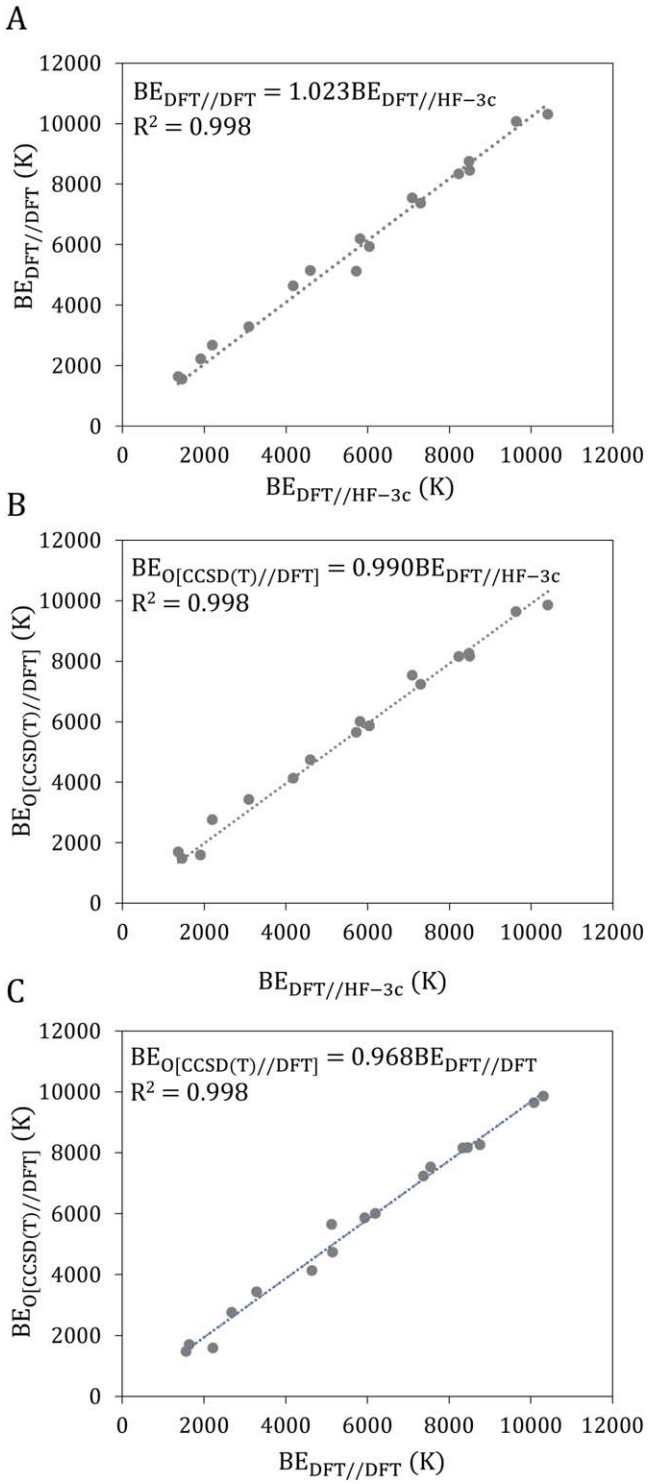

Figure 4. Linear fits between (A) the BE values computed at DFT//DFT vs. those at DFT//HF-3c level, (B) the BE values computed at O[CCSD(T)/DFT] level vs. those at DFT//HF-3c level, and (C) the BE values computed at O[CCSD(T)/DFT] level vs. those at DFT//DFT level. The linear fit equations are shown in the graphs.

3.1.3. BE Refinement at O[CCSD(T)//DFT]

As explained in Section 2.3, an ONIOM local approximation has been performed (O[CCSD(T)//DFT]) to assess the accuracy of the $BE_{DFT//DFT}$ and $BE_{DFT//HF-3c}$ values and, in the same time, to refine their values. This correction has been performed for all the species, with the exception of the HC_3N

Table 2
BE(0) Values (in Kelvin Units) Computed at DFT//HF-3c Level on the ASW Model

	CWS		ASW									
Species	DFT//HF-3c	DFT//DFT	1	2	3	4	5	6	7	8	9	10
N	1625	1891	1744	1514	370	3194	1643	905	1419	657	…	…
NH	3551	3945	2728	1167	2135	3792	4692	1167	2558	1469	…	…
NH_2	5134	5047	6722	3281	3712	5567	5714	5714	3792	3162	…	…
NH_3	6204	6265	7511	4476	5795	5039	5590	5181	4293	…	…	…
CN	…	…	6690	3677	2605	4171	7792	7471	3014	3431	…	…
HCN	4865	4354	2484	4354	3076	4364	2779	4977	5222	6306	…	…
HNC	7207	7440	6603	5527	4813	7932	10077	7200	4663	3820	…	…
N_2	1236	1329	1145	1451	1114	1012	756	…	…	…	…	…
NO	1163	1392	965	629	512	291	931	945	…	…	…	…
HNO	3909	4376	2346	2680	2214	2704	3144	3915	3329	2715	…	…
CH_3NH_2	7221	7184	5760	5649	6041	6932	4373	8293	6147	5039	…	…
CH_3CN	6025	6416	4920	6416	4328	7577	4956	7585	2623	3423	…	…
OCN	…	…	2635	1471	2216	1155	1816	1759	2370	1708	…	…
NH_2CN	8848	8763	7076	6556	7931	10,707	2503	9955	10,704	6554	5230	7367
HNCO[a]	6994	7087	5154	6932	4404	4386	7977	6485	4149	3390	…	…
N_2O	2628	2794	2162	1349	1989	3042	3923	2389	3043	1376	…	…
NH_2CHO	8186	8564	10,904	6357	8789	5795	7194	6009	5764	6214	…	…
NO_2	1869	2278	1833	1286	1467	1244	658	1088	…	…	…	…
HC_3N	3213	3287[b]	4092	2688	2954	6635	4784	6466	3715	1889	…	…
CH_2CHCN	4944	5268	4377	6411	4956	3978	6547	4956	2512	3900	…	…
HC_5N	…	…	8044	605	…	…	…	…	…	…	…	…

Notes.
BE(0) values at DFT//HF-3c and at DFT//DFT level for the CWS model are also included.
[a] The BE(0) values at DFT//HF-3c level have been computed using the DFT//PBE procedure; see Section 3.1.1.
[b] BE(0) value from the correlation between the BE(0) at DFT//DFT vs. DFT//HF-3c ones; see Figure 4.

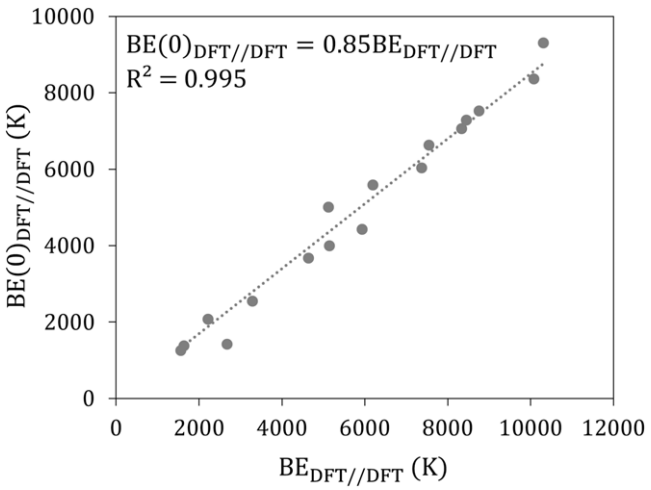

Figure 5. Linear fit between between BE(0)s and BEs computed at DFT//DFT level for adsorption at the CWS ice model. The linear fit equation is shown in the graph.

molecule, which gave energy convergence problems (vide supra).

Figures 4(B) and (C) show the correlation between the $BE_{O[CCSD(T)//DFT]}$ values against those computed at DFT//HF-3c and DFT//DFT, respectively. The linear fits show an overall perfect agreement. In conclusion, the DFT//DFT procedure is a reliable method to compute the BEs. In the same way, these results indicate that the cost-effective DFT//HF-3c procedure is a robust approach to obtain accurate BEs, which is relevant when dealing with the adsorption on ASW model, whose size prevent us from applying the DFT//DFT approach.

3.1.4. Zero-point Energy Correction

As mentioned in Section 2.3, for adsorption on the CWS model, we performed harmonic frequency calculations of a fragment consisting of the adsorbate and the binding site regions on the DFT-optimized structures. The resulting ZPE-corrections are used to correct the BE giving the final BE(0)s by means of Equation (4). The resulting BE(0) values are shown in Table 2, while Figure 5 shows the correlation between BE and BE(0) values. The linear fit is very good and shows that, to get BE(0), the raw BE values should be scaled by a factor of 0.85. The same scaling factor has been applied to correct the DFT//HF-3c BE values for the adsorption at the CWS model (see also Table 2) as well as to estimate the final BE(0) values for adsorption on the ASW model (see below).

3.2. BEs on the ASW

On the CWS model, the adsorption of the species was performed on only one (the unique) binding site due to the high symmetry of CWS structure. This is at a variance with the ASW model, which exhibits a variety of binding sites, therefore representing an ice model closer to the amorphous interstellar ice.

As already mentioned, for ASW, the BEs have been obtained at DFT//HF-3c level, and therefore, the final BE(0)s were computed by scaling the BE values by 0.85 (see Section 3.1.4), with the exception of the HNCO molecule, computed at the DFT//PBE level (see Section 3.1.1). Figures 3(C) and (D) show, as an example, the optimized geometries of adsorption at site 5 of the ASW for NO_2 (Hb-A group) and NH_2CN (Hb-AD group), respectively.

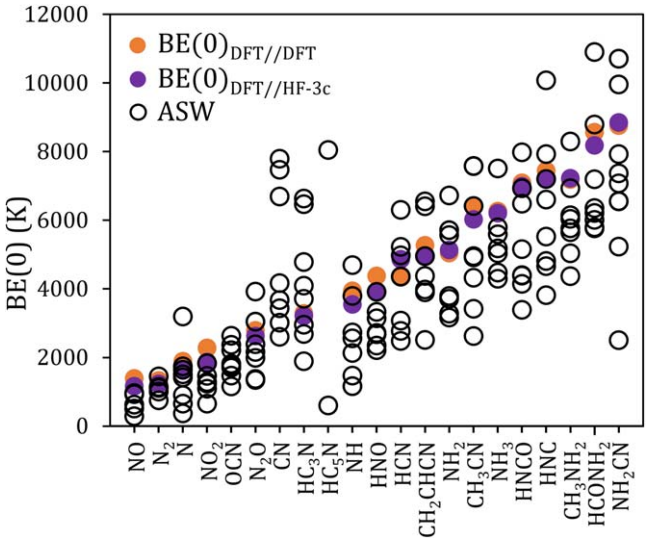

Figure 6. BE(0)s for all considered species on CWS (filled circles) and on ASW (empty circles) models. For ASW, BE(0) values at DFT//HF-3c. Multiple values for each species are for different adsorption sites.

On the ASW model, the adsorption of the species that were critical on the CWS model (i.e., CN, OCN, and HC_5N) converged smoothly.

For each of the considered N-containing species, at least five different BE values have been computed. For most of the cases, eight different BE values have been obtained, and for the particular case of NH_2CN, a total of 10 cases resulted. The exception is the HC_5N molecule (structure already problematic on the CWS model), for which only two BEs have been computed (which can be considered the upper and lower limits in its BE distribution). Table 2 shows the computed BE(0)s on the ASW model, to be compared with those from the CWS model.

Obviously, the BEs on the ASW model are different from those on the CWS model, as a result of a richer local environment for the ASW model (see Figure 6). This results in a wider range of BE values for each species on the ASW, compared to the CWS. Considering that a nonexhaustive unbiased search for all possible adsorbate positions at the ASW surface was not carried out, the present range of the BEs is somehow limited.

As a general trend, BEs computed on the CWS model are among the largest ones obtained for each species. Surface relaxation is more significant on the ASW model than on the CWS one due to the higher rigidity of the latter. The cost of surface relaxation decreases the final BE for ASW compared to CWS, in agreement with previous literature data (Ferrero et al. 2020; Perrero et al. 2022). Nevertheless, in most cases, the average BE value for the ASW is higher than the crystalline value, a trend that was already observed in Duflot et al. (2021).

Despite these differences, the general trend obtained in the BE values on the ASW is similar to that on the CWS: Hb-AD species develop larger BE values (between 605 and 10,904 K) than Hb-A species (between 291 and 4171 K). The reasons for these BE trends do not differ from those already raised for the CWS case (vide supra). The only exception to this trend is the CN molecule: despite belonging to the Hb-A group, three adsorption complexes exhibit higher BEs compared to the rest of the species of the same group (see entries 1, 5, and 6 of Table 2). For these cases, CN, rather than establishing H-bonds with the surface, forms a hemibonded system with an outermost water of the ice model, establishing a non-classical two-center three-electron bond (hemibond) between the unpaired electron on the carbon atom of CN and the lone pair electrons of the oxygen atom of the water surface (see the optimized geometries for these cases in Appendix E). These hemibonded interactions between CN and H_2O were already found as a first step toward the formation of interstellar formamide on water ice surfaces (Rimola et al. 2018).

3.3. Desorption Rate Preexponential Factors

As detailed in Section 2.4, the desorption rate preexponential factors as a function of the temperature for each N-bearing species have been determined using Equation (5). The preexponential factor curves, as a function of T, are shown in Appendix F. The needed parameters entering Equation (5) are shown in Table 3. Moreover, when the monolayer peak desorption temperature (T_{peak}) from experimental measurements is available, we computed the desorption rate preexponential factors for both CWS and ASW models. The principal moments of inertia for the optimized structures (at the very same theory level as for the adsorption complexes) of each species have been computed with the MOLDRAW program (Ugliengo et al. 1993), while using the symmetry point group to assess the symmetry degeneracy. In the CWS, the area per adsorbate species is 6.49×10^{-19} m^2, with the exception of HC_3N and CH_2CHCN species, for which the area is 1.30×10^{-18} m^2 due to the adoption of the 1×2 unit cell. In the ASW, the area per adsorbate species was fixed at the value of 2.04×10^{-18} m^2.

For the species N, NH_3, HCN, N_2, CH_3CN, and NH_2CHO, we have calculated the desorption rate preexponential factors for both models at the T_{peak} values reported by Minissale et al. (2022). The obtained values range from 10^{13} to 10^{20}, with variations depending on the specific species. In both CWS and ASW models, the preexponential factors differ by a factor of 3 due to the variation in the surface area A between the two surface models.

4. Discussion

4.1. Comparison of the BEs between N-bearing and N-free Species

In a previous work, Ferrero et al. (2020) computed the BEs of 21 species (15 of which not containing N atoms) absorbed on the same CWS and ASW models adopted here and using the same DFT//HF-3c procedure. The considered species span a wide range of chemical compounds, including simple molecules (H_2, N_2, O_2, CO, CO_2, OCS, HCl, HCN, CH_4, NH_3, H_2O, and H_2S), organic compounds ($HCONH_2$, H_2CO, HCOOH, CH_3OH, and CH_3CN), and four radical species (OH, NH_2, HCO, and CH_3). As a whole, more than half of them were oxygen-bearing (O-bearing) species. Likewise, Perrero et al. (2022) computed a distribution of BEs using the same icy models and the DFT//HF-3c approach for 17 S-bearing species, of which only one contains N-atoms (NS). The set of S-bearing species included eight closed-shell species (H_2S, H_2S_2, CS, CH_3SH, SO_2, OCS, H_2CS, and C_3), and nine radicals (NS, HS, HS_2, HCS, SO, S_2, C_4S, C_2S, and S). As we have adopted the same icy models and computational methods,

Table 3

Parameters Used for the Calculation of the Desorption Rate Preexponential Factors (ν, in per second) for Considered Species Adsorbed at CWS and ASW Ice Models: Mass m (in Atomic Mas Units), Symmetry Number (σ), Principal Moments of Inertia (Ix, Iy, and Iz, in Amu Å^2), and Experimental Monolayer Peak Desorption Temperatures (T_{peak}, in Kelvins) from Minissale et al. (2022) for Submonolayer Regimes on Compact ASW

Species	m	σ	I_x	I_y	I_z	T_{peak}	ν_{CSW}	ν_{ASW}	$\nu_{Minissale}$
N	14.01	1	⋯	⋯	⋯	35	7.61×10^{13}	2.39×10^{14}	1.17×10^{13}
NH	15.02	1	⋯	1.63	1.63	⋯	⋯	⋯	⋯
NH_2	16.02	2	1.09	2.25	3.34	⋯	⋯	⋯	⋯
NH_3	17.03	3	2.86	2.86	4.50	105	2.69×10^{16}	8.47×10^{16}	1.94×10^{15}
CN	26.02	1	⋯	17.34	17.34	⋯	⋯	⋯	⋯
HCN	27.03	1	⋯	17.97	17.97	137	4.05×10^{17}	1.27×10^{18}	1.63×10^{17}
HNC	27.03	1	⋯	39.44	39.44	⋯	⋯	⋯	⋯
N_2	28.01	2	⋯	14.12	14.12	35	2.75×10^{15}	8.65×10^{15}	4.51×10^{14}
NO	30.01	1	⋯	12.40	12.40	⋯	⋯	⋯	⋯
HNO	31.04	1	0.95	18.87	19.81	⋯	⋯	⋯	⋯
CH_3NH_2	31.06	1	8.30	36.39	37.90	⋯	⋯	⋯	⋯
CH_3CN	41.05	3	5.30	84.06	84.06	120	3.30×10^{18}	1.04×10^{19}	2.37×10^{17}
OCN	42.02	1	⋯	71.68	71.68	⋯	⋯	⋯	⋯
NH_2CN	42.04	3	3.06	77.95	79.41	⋯	⋯	⋯	⋯
HNCO	43.03	1	1.00	73.91	74.91	⋯	⋯	⋯	⋯
N_2O	44.01	1	⋯	66.32	66.32	⋯	⋯	⋯	⋯
NH_2CHO	45.04	3	11.17	66.22	77.39	176	5.13×10^{19}	1.61×10^{20}	3.69×10^{18}
NO_2	46.01	2	5.49	54.09	59.58	⋯	⋯	⋯	⋯
HC_3N	51.05	1	⋯	161.36	161.36	⋯	⋯	⋯	⋯
CH_2CHCN	53.06	1	15.88	150.35	166.22	⋯	⋯	⋯	⋯
HC_5N	75.07	1	⋯	546.48	546.48	⋯	⋯	⋯	⋯

Note. The desorption rate preexponential factors calculated in this study for both icy models are compared with those by Minissale et al. (2022).

we can consistently compare the BE distributions for oxygen-, sulfur-, and nitrogen-bearing molecules.

Figure 7 shows the distributions of the BE(0)s from Ferrero et al. (2020) and Perrero et al. (2022), which are compared with those from this work. To avoid bias in the comparison, the BEs of the N-bearing species reported by Ferrero et al. were excluded in the Ferrero's BE(0) plot.

The distribution of BEs provided by Ferrero et al. (2020) exhibits a bimodal character reminiscent of two distinct adsorption modes: (i) the group with low BEs, which includes simple molecules characterized by weak dispersive interactions; and (ii) the group with high BEs, which includes large size species involving both dispersive and strong H-bond interactions. In contrast, the distribution of BEs computed by Perrero et al. (2022) for the S-bearing species exhibits a unimodal-like behavior, with a relatively narrow range of BEs, due to a dominance of the dispersive interactions.

The distribution of BEs for N-bearing species spreads over a broad range of values, with a rather flat distribution, showing H-bonds as well as dispersive interactions as both relevant. Differences in the BEs are due to the different number and strength of H-bond interactions with the ice surface, resulting in a broad BE distribution.

A more detailed comparison has been performed for four N-bearing species (CN, OCN, NH, and NH_2) with their O-bearing (CO, CO_2, OH, and H_2O) and S-bearing (CS, OCS, SH, and H_2S) analogs. It is worth noting that all these N-bearing species are radicals while, in contrast, the oxygen and sulfur ones are closed-shell species, with the exception of OH and SH (analogs for NH), which are also radicals. Table 4 shows the calculated BE(0)s for these species, while Figure 8 represents the range of BE(0)s calculated for these species.

As a general trend, the BEs of the selected N-bearing species are similar to those for O- and S-containing analogs, as the nature of the interaction is similar. However, despite this general trend, some discrepancies emerge. H_2S molecule exhibits lower BEs compared to H_2O and NH_2 (the O- and N-analogs). This is because, in H_2S, dispersion interactions are the main driving forces in the adsorption (with weaker H-bonding, Perrero et al. 2022) while, in contrast, H_2O and NH_2 establish strong H-bonds with the icy surface, in addition to dispersion.

Regarding the CN species and its O- and N-analogs (CO and CS), the former species presents significantly larger BEs than CO and CS. This difference can be attributed to the formation, in three cases, of hemibonded systems between the CN species and icy water molecules, leading to increased BEs (as mentioned in Section 3.2). Beside the hemibonded complexes, the set of CN BEs on the ASW follows a BE distribution similar to that of CO and CS.

The above considerations raise a warning: it is always risky to guess a BE of a species by using the computed BE values of analogous species (CS versus CO as an example), as it is difficult to extrapolate dispersion and H-bonding contributions from the values of analogous species to guess those for the unknown species.

4.2. Comparison of the BEs with Literature Values

The computed BE(0)s are compared with available data from the literature, including experimental and computational studies. Table 5 and Figure 9 summarize the available data. Please note that we considered here the compilations where more than one BE is reported, namely, the work by Das et al. (2018), Bovolenta et al. (2022), Minissale et al. (2022, 2022), and Wakelam et al. (2017).

4.2.1. Comparison with Experimental Works

Let us first compare our computed BE(0)s with those obtained experimentally. It is worth reminding that, while

Table 4
BE(0)s (in Kelvin Units) for Selected Di-atomic and Tri-atomic N-bearing Species and Their Oxygen- and Sulfur-bearing Analogs (Ferrero et al. 2020; Perrero et al. 2022; See Text), Computed at DFT//HF-3c

N-bearing Species				O-bearing Species				S-bearing Species			
Species	CWS	ASW_{min}	ASW_{max}	Species	CWS	ASW_{min}	ASW_{max}	Species	CWS	ASW_{min}	ASW_{max}
CN	…	2605	7792	CO	1663	1109	1869	CS	2453	995	3680
OCN	…	1155	2635	CO_2	2568	1489	2948	OCS	2405	1286	2861
NH	3551	1167	4692	OH	5588	1551	5321	SH	2799	1078	4313
NH_2	5134	3162	6722	H_2O	7200	3605	6111	H_2S	4033	1970	4489

Note. For the ASW model, only the minimum and maximum BE(0)s are reported.

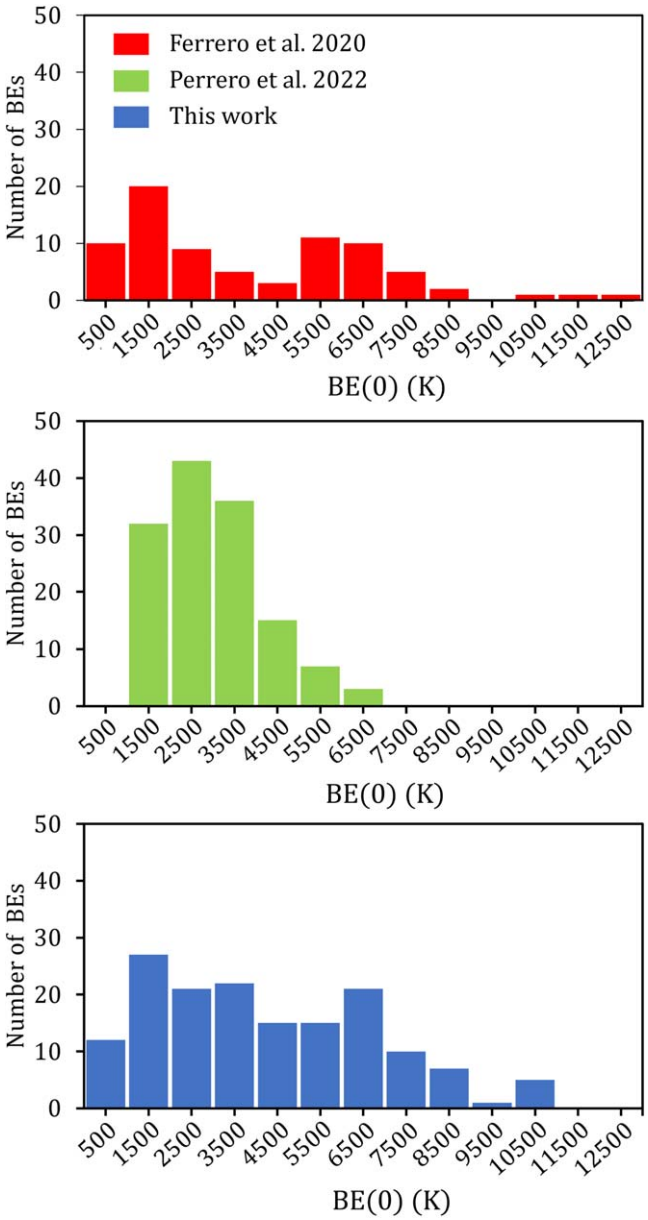

Figure 7. Distribution of the BE(0)s computed on the ASW model using the DFT//HF-3c methodology for N-bearing species (blue), the non-N-bearing species considered in Ferrero et al. (2020; red), and the S-bearing in Perrero et al. (2022; green).

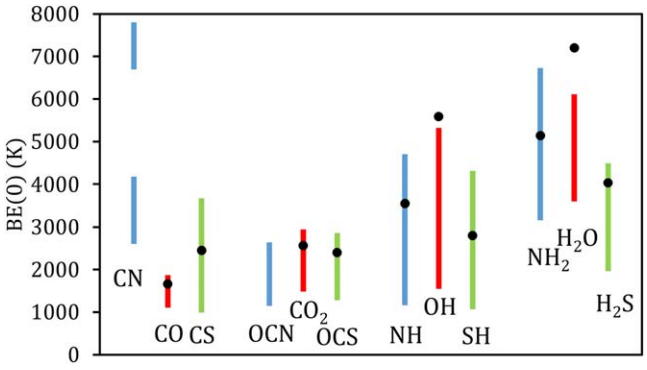

Figure 8. Comparison of BE(0)s for selected di-atomic and tri-atomic N-bearing species and their oxygen and sulfur analogs (Ferrero et al. 2020; Perrero et al. 2022; see text). Solid lines cover the ranges between the minimum and maximum BE(0)s computed on the ASW at DFT//HF-3c for N- (blue), O- (red), and for S- (green) bearing species. The range of BE(0)s for the CN species is divided between cases in which a hemibond is formed (top range) and those in which a hemibond is not formed (bottom range). For reference, also the BE(0)s on the CWS computed at DFT//HF-3c level are reported (filled black circles).

computational calculations directly provide BE(0) values, TPD experiments estimate desorption energies, which are derived from the desorption rate preexponential factor curves. Among other problems, the difference arises because desorption energies are surface coverage dependent, and hence, the comparison between computational BE(0)s and desorption energies is not totally straightforward (e.g., Ferrero et al. 2022; Minissale et al. 2022). In our case, we always simulate a zero coverage limit, at least for the ASW model, while higher coverages are implied by the smaller unit cell of the CWS model.

Considering these caveats, we compare our BE(0)s with those provided in the compilation taken from Minissale et al. (2022), where the authors report a list of BE(0)s and preexponential factors extracted by experimental works and carefully reviewed for 21 relevant species. Of these, only N, NH_3, HCN, N_2, CH_3CN, and NH_2CHO are comparable with the present results. As already pointed out, we focus on the recommended BEs in the submonolayer regimes on compact ASW. As one can see from Table 5, all the Minissale's recommended BE(0)s fall within the range of our computed BE(0)s.

4.2.2. Comparison with Previous Theoretical Works

The easiest and cheapest method for computing the BEs was done in Wakelam et al. (2017). They assumed that a real BE value can be worked out assuming a single water molecule as an icy model. Neither ZPE nor BSSE corrections were added to the BEs. To compensate for the limitation of using a single water molecule to mimic the ice, a scaling factor was derived

Table 5
Summary of the Binding Energies (in Kelvins) Computed in the Present Work and Those from Literature Compilations

Species	BE(0)s from This Work			Binding Energies from Literature				
	CWS	ASW_{min}	ASW_{max}	$BE(0)_{Duflot}$[c]	$BE(0)_{Bovolenta}$[d]	$BE(0)_{Minissale}$[e]	BE_{Das}[f]	$BE_{Wakelam}$[g]
N	1625	370	3194	$\langle 359\rangle_{cry}$ / $\langle 580\rangle_{am}$	⋯	806	619	720
NH	3551	1167	4692	$\langle 2715\rangle_{cry}$ / $\langle 2437\rangle_{am}$	⋯	⋯	⋯	2600
NH_2	5134	3162	6722	⋯	3488 ± 265	⋯	3240	3200
NH_3	6204	4293	7511	$\langle 4468\rangle_{cry}$ / $\langle 4305\rangle_{am}$	3347 ± 219 // 1104 ± 197	5362	5163	5600
CN	⋯	2605	7792	⋯	⋯	⋯	1736	2800
HCN	4865	2484	6306	⋯	2425 ± 483 // 1899 ± 167	5344	2352	3500
HNC	7207	3820	10077	⋯	4628 ± 706 // 2552 ± 117	⋯	5225	3800
N_2	1236	756	1451	⋯	637 ± 114[b]	1074	1161	1100
NO	1163	291	965	⋯	⋯	⋯	1988	1600
HNO	3909	2214	3915	⋯	⋯	⋯	2988	3000
CH_3NH_2	7221	4373	8293	⋯	⋯	⋯	4434	⋯
CH_3CN	6025	2623	7585	⋯	⋯	6253	3786	4680
OCN	⋯	1155	2635	⋯	⋯	⋯	⋯	⋯
NH_2CN	8848	2503	10707	⋯	⋯	⋯	⋯	⋯
HNCO	6994[a]	3390[a]	7977[a]	⋯	⋯	⋯	5554	4400
N_2O	2628	1349	3923	⋯	⋯	⋯	⋯	⋯
NH_2CHO	8186	5764	10904	⋯	⋯	9561	⋯	6300
NO_2	1869	658	1833	⋯	⋯	⋯	⋯	⋯
HC_3N	3213	1889	6636	⋯	⋯	⋯	2925	⋯
CH_2CHCN	4944	2512	6547	⋯	⋯	⋯	⋯	⋯
HC_5N	⋯	605	8044	⋯	⋯	⋯	⋯	⋯

Notes. Second column reports the BE(0)s computed in this work for the CWS model at DFT//HF-3c level. Third and fourth columns report the minimum and maximum BE(0)s computed in this work for the ASW model. Fifth to eighth columns report the binding energies from the literature, as indicated in the header.
[a] BE(0)s have been computed using the DFT//PBE method.
[b] It does not include ZPE correction.
[c] Duflot et al. (2021), calculated average values on crystalline (*cry*, left) and amorphous (*am*, right) surface models.
[d] Bovolenta et al. (2022), two values indicate bimodal character in the BE(0) distribution.
[e] Minissale et al. (2022).
[f] Das et al. (2018).
[g] Wakelam et al. (2017).

from fitting the experimental BEs versus the computed BE ones for 16 species. In general, the final BEs by Wakelam et al. lay within the range of our computed BEs, although in the lower limit of our range (see Figure 9). The adoption of a single water molecule as an ice surface model cannot account for the double behavior of H-bond donor and H-bond acceptor of some species, neglecting the H-bond cooperativity.

Das et al. (2018) presented BEs by computing interaction energies of species on icy cluster models of four or six water molecules. As for the Wakelam et al. study, neither ZPE nor BSSE corrections were considered. Overall, the Das et al. BEs are within the range of the BEs computed in the present work, with similar considerations for the Wakelam et al. case. We believe these clusters are still too small to allow H-bonding cooperativity to be at its best.

Duflot et al. (2021) computed a set of BEs for different astrochemical species, among them N, NH, and NH_3 ones. These authors combined force field MD simulations with quantum chemical calculations for various snapshots taken along the MD trajectory. With the ONIOM procedure (combining DFT with semiempirical methods), the authors computed BE(0)s on crystalline and amorphous cluster models comprising 120–150 atoms. The averaged set of calculated BE values, are also reported in Table 5. For a proper comparison with the present data, we averaged the BE(0)s for the N, NH, and NH_3 species, getting $\langle 1431\rangle$, $\langle 2464\rangle$, and $\langle 5412\rangle$ K, showing the Duflot's BEs to differ by some amount with the present ones. Although the cluster models adopted by Duflot et al. (2021) are more realistic and bigger than the minimal ones used in Wakelam et al. (2017) and Das et al. (2018), the same trend (although less pronounced) is observed: the Duflot's values lay in the lower part of our range. The reasons of these differences are difficult to assess, as different surface models (cluster versus periodic), quantum chemical methods, and computational strategies (ONIOM approach versus DFT//HF-3c) were adopted. Furthermore, as the comparison is done for only three species, it is difficult to arrive at definite conclusions.

Bovolenta et al. (2022) adopted a different approach by presenting BE(0) distributions consisting of 225–250 values for 21 interstellar molecules on different amorphous cluster models made up by 22 water molecules. A three-step computational procedure was employed, involving sampling, geometry optimization at HF-3c level, and BE(0) calculation at DFT level of theory. Average values and standard deviations were obtained from a Gaussian fit of the set of BE(0)s. If a bimodal character was present in the distribution of BE(0)s, two Gaussian fits were used. Only five of the Bovolenta et al. species (that is, N_2, HCN, NH_2, NH_3, and HNC) coincide with our set of compounds (see Table 5), making it hard to assess a general trend. Additionally, it is noteworthy that, for the purpose of comparison, we are providing the minimum/maximum of each BE(0) value, while Bovolenta et al. provides average values and standard deviations. For species presenting low BE(0)s (namely, N_2, HCN, NH_2), our results align very well with the Bovolenta's values. However, discrepancies arise for species presenting large BE(0)s (namely, NH_3 and HNC), in

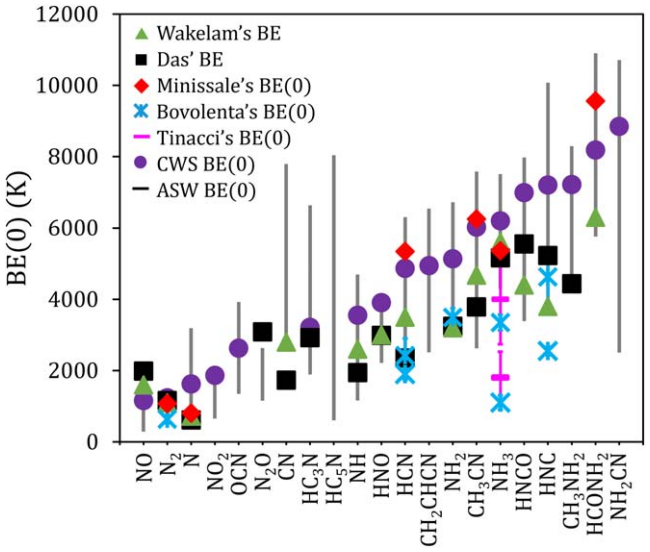

Figure 9. Comparison of the binding energies computed in this work and those from literature compilations. The solid gray lines show the range between the minimum and maximum BE(0)s computed on the ASW model while the filled purple circles are for the BE(0)s computed on the CWS model at DFT//HF-3c level. The light blue crosses correspond to the mean values from the Gaussian fit of BE(0)s distributions reported by Bovolenta et al. (2022), showing also the standard deviations. The pink lines correspond to the peaks of Maxwell–Boltzmann distribution functions of BE(0)s distribution reported by Tinacci et al. (2023), along with the standard deviations. For the other cases, only one value has been given: BE(0)s reported by Minissale et al. (2022; red diamonds), BEs reported by Das et al. (2018; black squares), and BEs reported by Wakelam et al. (2017; green triangles).

which the Bovolenta's BEs fall below the range of our computed BE(0)s. This could be due to the large size and amorphous nature of our ASW model, showing richer morphological features (including cavities), compared to the compact nature of the cluster models adopted by Bovolenta et al., thereby affecting the limit values of the BE distributions. As already pointed out in Bovolenta et al., adsorption on sites presenting a cavity will give larger BE(0)s compared to those for flat adsorption sites. An additional factor that can affect the comparison is the effect of the ZPE correction, which decreases the BE values by about 25% in the Bovolenta et al. work, at a variance with the 15% as a maximum in our case.

Within a context of prebiotic chemistry, Tóth Ugyonka et al. (2024) recently computed the adsorption of HCN on low density amorphous water ice model by means of grand canonical Monte Carlo simulations based on classical force fields at the temperatures of 50, 100, and 200 K. Their heat of adsorption computed at an infinitely low surface coverage were -49.4 ± 3.9 kJ mol^{-1} (BE(0) of 5941 ± 469 K). This range is well within our computed one for HCN, despite the differences between the surface models and methodological aspects.

Finally, Tinacci et al. (2022) reported a study of the NH_3 BE(0)s obtained on an amorphous water ice model (roughly spherical) composed by 200 water molecules, the largest so far reported in the literature (Germain et al. 2022). These authors characterized 77 unique NH_3 structures on the icy grain, and, consequently, a BE(0) distribution was derived covering a wide range of values, from 1500 to 6000 K. Remarkably, the NH_3 BE(0) distribution exhibited a bimodal shape, with a first peak at around 4000 K and the second one, unexpected and never seen before by other studies, at 1800 K. As in previous works (Ferrero et al. 2020; Duflot et al. 2021), the range of NH_3 BEs (0) computed here, 4293–7511 K, only covers the highest values of the BE distribution by Tinacci et al., likely because the ASW model is too small to have adsorbing sites with such a low BE (see also the discussion in Tinacci et al. 2022).

In a subsequent work, Tinacci et al. (2023) computed the H_2O BE(0) distribution on the same 200 water molecule grain model. Contrarily to NH_3, the water BE(0)s distribution exhibits a single peak at 4230 K and covers the range 1700–7400 K, while Ferrero et al. (2020), with the same ice model employed here, estimated a range, 3600–6111 K, rather shifted toward the high BEs. Also, in this case, therefore, the Ferrero et al. model missed sites with small BE values, even though the disagreement is much less important than that with ammonia, where the whole low-BE tail is missed. Therefore, the case of ammonia should not be generalized, and not all species have a low-BE second peak. The above considerations provide an important take-home message: the size of the icy model matters, especially when providing adsorption sites characterized by small BE values. We believe this is because large water clusters tend to maximize the number of internal H-bonds, leaving less available strong adsorption sites for the adsorbates. Small icy models, on the contrary, show too many "unsatisfied" water molecules at their surface, pushing up (higher-BE(0) values) their affinity toward adsorbates.

4.3. Comparison of the Desorption Rate Preexponential Factors

Our computed desorption rate preexponential factors are compared with those reported in the literature by Minissale et al. (2022), in Table 3.

In Minissale et al. (2022), the reported preexponential factors were computed using the Tait et al. (2005) formula, as in this work. However, some parameters are different. These are (i) the area per absorbed site, and (ii) the inertia moments. Regarding the area per adsorbed site, those for the CWS and ASW models were calculated according to their unit cell parameters, while in Minissale et al. a fixed value of 10^{-19} m^2 was used. This area is of the same order of magnitude of that of our CWS model (6.49×10^{-19} m^2), but 1 order of magnitude different from that of the ASW model (2.04×10^{-18} m^2). While the inertia moments were computed with the MOLDRAW program (Ugliengo et al. 1993; vide supra), Minissale et al. used the structures available in the ChemSpider[4] database, giving rise to some differences with our results.

Table 3 shows that the Minessale et al. derived ν values differ by up 2 orders of magnitude (our values being always larger than the Minissale's ones) due to the above described differences. Notably, smaller species exhibit lower differences between our and Minissale's preexponential factors, while larger molecules present more pronounced differences.

Given the key role of the desorption rate preexponential factors in determining the BE(0)s by inversion of Equation (5), accuracy in its quantification becomes imperative. Ultimately, even minor differences in the input parameters in computing a preexponential factor can lead to substantial variations in its value, and consequently to the experimentally derived BE(0) value.

[4] www.chemspider.com

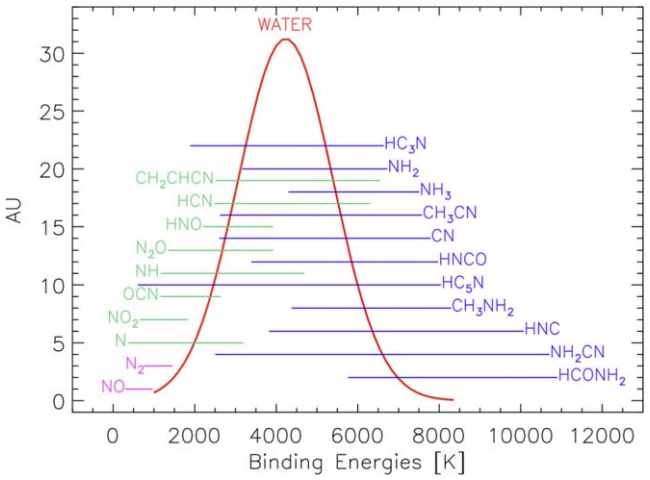

Figure 10. Comparison of the N-bearing species BEs computed in the present work with the distribution of water BEs computed by Tinacci et al. (2023; red curve). The bars represent the BE ranges of species belonging to groups 1 (magenta), 2 (blue), and 3 (green), defined in the text.

4.4. Astrophysical Implications

As emphasized in the Introduction, BEs have a direct impact on the interstellar chemistry, i.e., the chemical composition of the molecular ISM and its evolution. Indeed, BEs directly determine the dust temperature at which species, frozen on dust grains, sublimate. Such a process is mathematically expressed as being exponentially proportional to BEs (see, e.g., the reviews by Minissale et al. 2022; Ceccarelli et al. 2023). Therefore, even small variations can result in significant differences in sublimation temperatures, which can lead to large differences in species abundances in the gas-phase and on the dust grains.

Particularly important in the context of planetary formation is the case of protoplanetary disks: if a species is in the solid form, it will be available for planetesimal accretion, contributing to the formation of rocky objects such as planets or asteroids. However, if a species is in the gas-phase, elements contained within the species are more likely to become part of the forming of giant gaseous planets (e.g., Dodson-Robinson et al. 2009; Öberg & Bergin 2021).

In protoplanetary disks, snow lines are the regions where gaseous species freeze out onto dust grains (e.g., Hartmann et al. 2017; Öberg & Bergin 2021). The locations of snow lines depend on both the dust temperature and the BE of the frozen species. In general, moving farther from the center of the disk, the dust temperature decreases, and consequently, species with low BEs remain gaseous at larger distances from the disk center, while those with larger BEs freeze out onto dust grains closer to the center disk. As a result, snow lines (and therefore BEs) have a direct relation on the gaseous versus solid chemical composition in protoplanetary disks, playing a crucial role in the chemical composition of the rocky/gaseous objects being formed in those regions (e.g., Öberg et al. 2011; Öberg & Wordsworth 2019; Mollière et al. 2022).

Within this context, it is interesting to compare the BEs of the N-containing species with those of water, since water is crucial for the emergence of life. In practice, the point is to know which N-bearing species are frozen or gaseous within the water snow line. As mentioned in the previous section, Tinacci et al. (2023) computed the BE distribution on a 200 water molecule amorphous ice model and found that it follows a Gaussian distribution with a peak at 4230 K. Tinacci et al. (2023) also introduced the water BE distribution in a model of a protoplanetary disk and showed the influence of the BE distribution on the water snow line with respect to the radius assuming a single value. They also estimated the water content of possible planetesimals at a different distance from the disk center. Explicitly modeling the N-chemistry in a protoplanetary disk is beyond the scope of the present work, but we can still give order of magnitude arguments about what N-species will likely be part of planetesimals that are also enriched with water.

Figure 10 shows the ranges of the calculated BEs for the N-bearing species compared to the BE distribution of water (Tinacci et al. 2023). We can identify three groups of N-bearing species:

1. *The N-species that will completely sublimate in regions where 96% of water is frozen, namely, whose maximum BE is lower than ∼1700 K: N_2 and NO.* These species will not be incorporated into the planetesimals. Note that N_2 is expected to be among the major nitrogen reservoirs.
2. *The N-species that (at least a fraction) remains frozen also in regions where 96% of water has completely sublimated, namely, whose maximum BE is larger than ∼6500 K: CN, NH_2, HNC, NH_3, HNCO, HC_3N, NH_2CN, CH_3CN, $HCONH_2$ (indicated as NH_2CHO in astrochemical works), CH_3NH_2, and HC_5N.* These species will very likely be incorporated into water-rich planetesimals. It is particularly important for the case of ammonia, whose large fraction remains frozen in water-rich ices, and which is also a major nitrogen reservoir, with the caveat of a small low-BE tail not caught by our computations (see the discussion in Section 4; and Tinacci et al. 2022). Also interesting are the cases of HNCO and NH_2CHO, which contain the four elements CHON important for biological chemistry and are fully conserved as frozen molecules in the eventual planetesimals. In particular, formamide has been evoked as a crucial molecule that can lead to the formation of a multitude of prebiotic species (e.g., Saladino et al. 2012b), and, for this reason, its chemistry has been the focus of numerous works (see, e.g., the review by López-Sepulcre et al. 2019).
3. *All the other species in between, namely, those that have at least a fraction frozen in a region where more than 4% and less than 96% of water is frozen: N, NH, HCN, HNO, OCN, N_2O, NO_2, and CH_2CHCN.* Among these species, it is worth noticing that much of HCN and CH_2CHCN will be preserved in water-rich ices incorporating eventual planetesimals. In particular, HCN has been invoked as the most important brick leading to the formation of amino acids and nucleic acid bases (Oró 1960; Santalucia et al. 2022).

To sum up, the accurate quantification of BEs is crucial to accurately describe snow line positions when modeling planet formation. The distribution of BE directly affects the chemical composition of the forming rocky objects, as it determines which species remain in the gaseous phase and which ones are frozen out onto dust grains.

5. Conclusions

In this work, we computed quantum mechanically the BEs of 21 N-bearing species of astrochemical relevance (14 closed-shell

species and seven radicals) absorbed on two water ice models mimicking the mantle of interstellar ice grains. Two icy models are defined within the periodic boundary conditions, simulating a crystalline proton-ordered ice (CWS model) and an amorphous one (ASW model). The BEs have been computed on the larger ASW model with the cost-effective DFT//HF-3c procedure, in which the structure of the adsorbate/(icy grain) is relaxed at HF-3c level, followed by the punctual energy evaluation at full DFT level, i.e., B3LYP-D3(BJ)//HF-3c (closed-shell species) or M06-2X//HF-3c (open-shell species). The performance of this methodological scheme was validated on the CWS model, showing an excellent correlation with the BEs computed at DFT//DFT level and even when comparing BEs resulting from a more refined ONIOM correction at CCSD(T) level.

We proved that molecules exhibiting both H-bond acceptor and donor character (Hb-AD group) bind with higher-BE values than those with only H-bond acceptor character (Hb-A group). The CWS model has only one adsorption site due to symmetry constraints, resulting in a single BE value for each species. This is in contrast with the ASW model, exhibiting a sensitive number of different surface sites, giving rise to a range of BEs for each species. BEs computed for the CWS model are usually in the higher side of the BEs distributions computed for the ASW model. This is due to a better hydrogen bond cooperativity for the crystalline CWS model compared to the ASW one and, due to the rigidity of the CWS model, to a smaller deformation cost suffered by the icy surface due to the adsorption.

The smallest DFT//HF-3c computed BE value is for NO while the higher are for NH_2CHO and NH_2CN, in agreement with their double H-bonding donor/acceptor character. The BE distribution (500–12,500 K) is featureless and broader than the analogous oxygen-bearing molecules computed by Ferrero et al. (2020), in which a bimodal shape resulted. For sulfur-containing molecules, as computed by Perrero et al. (2022), the BE distribution is single peaked spanning much narrower BE values (1500–6500 K) than the present one. Computed BEs have been compared with experimental and computational data available from the literature.

Previous BEs from theory overlap the range of our BEs, although they correspond to the lower part of our range due to the adoption of different icy models, which span from minimal clusters (Wakelam et al. 2017; Das et al. 2018; Hendrix et al. 2023) to more developed clusters and periodic systems (Duflot et al. 2021; Bovolenta et al. 2022; Germain et al. 2022; Tinacci et al. 2022; Tóth Ugyonka et al. 2024). Experimentally, the BEs obtained through the mathematical manipulation of the TPD spectra (Ferrero et al. 2022; Minissale et al. 2022) are in fairly good agreement with our computed results.

Finally, the computed BEs have been used to predict which N-bearing molecules can remain frozen in the protoplanetary disk region where also water is frozen and can potentially be incorporated into the water-rich planetesimals that will eventually form a rocky planet. We found that two important N-species, HCN and NH_2CHO, which have a particularly important prebiotic potential (Oró 1960; Saladino et al. 2012b; Santalucia et al. 2022), will likely be incorporated in those water-rich planetesimal ices.

Acknowledgments

This project has received funding from the Marie Sklodowska-Curie for the project "Astro-Chemical Origins" (ACO), grant agreement No. 811312, and within the European Union's Horizon 2020 research and innovation program from the European Research Council (ERC) for the projects "The Dawn of Organic Chemistry" (DOC), grant agreement No. 741002, and "Quantum Chemistry on Interstellar Grains" (QUANTUMGRAIN), grant agreement No. 865657. MICIN (projects PID2021-126427NB-I00 and CNS2023-144902) is also acknowledged. The Italian Space Agency for cofunding the Life in Space Project (ASI N. 2019-3-U.O), the Italian MUR (PRIN 2020, Astrochemistry beyond the second period elements, Prot. 2020AFB3FX) are also acknowledged for financial support. Support from the Project CH4.0 under the MUR program "Dipartimenti di Eccellenza 2023-2027" (CUP: D13C22003520001) is also acknowledged. The authors thankfully acknowledge RES resources provided by BSC in MareNostrum to activities QHS-2022-3-0007 and QHS-2023-2-0011, and the supercomputational facilities provided by CSUC.

Appendix A
Computational Details

We adopted computational parameters used in Ferrero et al. (2020) for optimization and frequency calculations. To sample the reciprocal space, the Pack-Monkhorst mesh was adopted. For the crystalline ice, the SHRINK factor was set to 2 resulting in four K-points in the first Brillouin zone. For the amorphous ice, the SHRINK factor was set to 1, resulting in two K-points in the first Brillouin zone. The threshold parameters for the evaluation of the Coulomb and exchange bielectronic integrals (TOLINTEG) were set to 7, 7, 7, 7, and 14 for both models, the crystalline and the amorphous ices. Some species required the use of BROYDEN accelerator for the convergence of the SCF. Integration grid (XLGRID) was added and fixed to default values.

Appendix B
BE Detailed Calculation

B.1. BBSE-corrected Interaction Energies

BEs are calculated from the interaction between a surface, S, in this case represented by a slab model, and the adsorbed molecular species, μ,

$$\Delta E = E_P(S\cdot\cdot\mu\,//\,S\cdot\cdot\mu) - E_P(S\,//\,S) - E_M(\mu\,//\,\mu) \quad \text{(B1)}$$

where E_Z (xy//x′y′) stands for the energy of the species xy in the optimized geometry x'y', and M and P stand for molecular or periodic calculations. In this case, E_P (S··μ//S··μ) is the energy of the species adsorbed on the surface in its optimized geometry, E_P (S//S) is the energy of surface, and E_M (μ//μ) stands for the energy of the optimized single species.

This equation does not consider some factors such as the deformation of S and the μ, the BSSE, or lateral interactions between μ of different unit cells. Some corrections must be done to obtain the corrected interaction energy. First, the deformation of both the slab model and the species must be quantified.

$$\delta E_S = E_P(S\,//\,S\cdot\cdot\mu) - E_P(S\,//\,S). \quad \text{(B2)}$$

$$\delta E_\mu = E_P(\mu\,//\,S\cdot\cdot\mu) - E_M(\mu\,//\,\mu). \quad \text{(B3)}$$

So, the deformation-free interaction energy ΔE^* is defined as

$$\Delta E^* = E_P(S \cdot\cdot \mu // S \cdot\cdot \mu) - E_P(S // S \cdot\cdot \mu) - E_P(\mu // S \cdot\cdot \mu). \quad \text{(B4)}$$

Due to the use of a finite basis set, BSSE arises, which must be corrected, in this case, adopting the Boys–Bernardi CP correction (Boys & Bernardi 1970).

$$\mathrm{BSSE}(S) = E_P(S \cdot\cdot [\mu] // S \cdot\cdot \mu) - E_P(S \cdot\cdot \mu // S \cdot\cdot \mu), \quad \text{(B5)}$$

$$\mathrm{BSSE}(\mu) = E_P([S] \cdot\cdot \mu // S \cdot\cdot \mu) - E_P(S \cdot\cdot \mu // S \cdot\cdot \mu), \quad \text{(B6)}$$

where E_Z (x[y]//x′y′) is the energy of the x species in the presence of the ghost functions of the y species computed in the geometry optimization of the x′y′.

The last correction corresponds to the lateral interaction δE_L due to interaction between species of different unit cells.

$$\delta E_L = E_P(\mu // S \cdot\cdot \mu) - E_M(\mu // S \cdot\cdot \mu). \quad \text{(B7)}$$

Thus, BSSE-corrected interaction energies considering all these corrections can be expressed as

$$\Delta E^{CP} = \Delta E^* + \delta E_S + \delta E_\mu + \delta E_L - BSSE(S) - BSSE(\mu). \quad \text{(B8)}$$

BEs are positive values and are defined as the absolute value of ΔE^{CP} and including the corresponding ZPE correction.

$$\mathrm{BE} = |\Delta E^{CP}| - \Delta\mathrm{ZPE} \quad \text{(B9)}$$

in which the ZPE correction ΔZPE is computed as

$$\Delta\mathrm{ZPE} = \mathrm{ZPE}(S \cdot\cdot \mu\mu) - \mathrm{ZPE}(S) - \mathrm{ZPE}(E_M). \quad \text{(B10)}$$

Appendix C
Dispersion Contribution

Dispersive contributions for BSSE-corrected interaction energies can be quantified for closed-shell species. For open-shell species and due to the nature of M06-2X species, dispersive contributions cannot be separated from total BEs. Table 6 shows BSSE-corrected interaction energies, dispersion contributions, and their percentages for all closed-shell species. All cases computed on the ASW are included as well as the ones computed on the CWS at DFT//HF-3c and at DFT//DFT methodologies.

Table 6
Computed BEs on the ASW at DFT//HF-3c Level and on the CWS at DFT//HF-3c and at DFT//DFT Level for Closed-shell Species

		CWS		ASW									
Species		DFT//HF-3c	DFT//DFT	1	2	3	4	5	6	7	8	9	10
NH_3	BE	7301	7373	8840	5268	6820	5930	6579	6098	5052	…	…	…
	Disp	1816	1852	2917	843	2864	1838	1118	1768	758	…	…	…
	Disp (%)	25	25	33	16	42	31	17	29	15	…	…	…
HCN	BE	5725	5124	2923	5124	3620	5136	3271	5857	6146	7421	…	…
	Disp	3043	2057	1111	2357	1050	2208	1308	3456	2458	1633	…	…
	Disp (%)	53	40	38	46	29	43	40	59	40	22	…	…
HNC	BE	8482	8756	7772	6504	5664	9335	11,860	8473	5488	4496	…	…
	Disp	3280	2936	2019	3372	2844	3042	2293	3037	2488	766	…	…
	Disp (%)	39	34	26	52	50	33	19	36	45	17	…	…
N_2	BE	1455	1564	1347	1708	1311	1191	890	…	…	…	…	…
	Disp	1636	1636	1859	2255	1377	1763	409	…	…	…	…	…
	Disp (%)	112	105	138	132	105	148	46	…	…	…	…	…
HNO	BE	4601	5150	2761	3154	2606	3182	3700	4608	3917	3196	…	…
	Disp	1556	1339	1524	649	705	1135	1231	1748	1321	1135	…	…
	Disp (%)	34	26	55	21	27	36	33	38	34	36	…	…
CH_3NH_2	BE	8498	8455	6779	6648	7110	8158	5146	9760	7234	5930	…	…
	Disp	3060	2918	2545	1345	1597	2882	992	4095	2300	1764	…	…
	Disp (%)	36	35	38	20	22	35	19	42	32	30	…	…
CH_3CN	BE	7090	7551	5790	7551	5094	8918	5465	8926	3088	4029	…	…
	Disp	3373	3090	3381	1962	2537	4612	2038	4601	2818	1326	…	…
	Disp (%)	48	41	58	26	50	52	37	52	91	33	…	…
NH_2CN	BE	10,413	10,312	8327	7716	9334	12,601	2946	11,716	12,597	7713	6155	8670
	Disp	3478	3164	1759	1293	2034	5560	619	1811	5571	3975	1480	2991
	Disp (%)	33	31	21	17	22	44	21	15	44	52	24	34
HNCO[a]	BE	8232	8340	6066	8158	5183	5162	9388	7632	4883	3989	…	…
	Disp	3079	2944	1692	2251	2682	2727	3956	2486	2187	1073	…	…
	Disp (%)	37	35	28	28	52	53	42	33	45	27	…	…

Table 6
(Continued)

Species		CWS		ASW									
		DFT//HF-3c	DFT//DFT	1	2	3	4	5	6	7	8	9	10
N_2O	BE	3092	3288	2544	1588	2340	3580	4617	2811	3581	1620	…	…
	Disp	2552	2484	2690	1015	1689	2802	2148	2807	2802	1084	…	…
	Disp (%)	83	76	106	64	72	78	47	100	78	67	…	…
NH_2CHO	BE	9634	10,079	12,833	7481	10,344	6820	8467	7072	6783	7313	…	…
	Disp	3560	3608	4107	2244	4862	1296	3979	2051	3052	1389	…	…
	Disp (%)	37	36	32	30	47	19	47	29	45	19	…	…
HC_3N	BE	3781	…	4816	3163	3477	7808	5630	7610	4373	2223	…	…
	Disp	3707	…	3941	2340	1224	4566	1764	4550	4327	710	…	…
	Disp (%)	98	…	82	74	35	58	31	60	99	32	…	…
CH_2CHCN	BE	5818	6199	5151	7545	5832	4682	7705	5832	2957	4590	…	…
	Disp	3356	3350	3448	3032	4028	4718	1869	2065	2197	3448	…	…
	Disp (%)	58	54	67	40	69	101	24	35	74	75	…	…
HC_5N	BE	…	…	9467	712	…	…	…	…	…	…	…	…
	Disp	…	…	4489	726	…	…	…	…	…	…	…	…
	Disp (%)	…	…	47	102	…	…	…	…	…	…	…	…

Note.
[a] BEs have been computed using the DFT//PBE method as an alternative to the DFT//HF-3c procedure; see Section 3.1.1.

Appendix D
Deformation Energies

The deformation energies of the surface and of the species are reported in Table 7.

Table 7
Deformation Energies of the Surface (δE_S) and of the Species (δE_μ) Computed on the ASW at DFT//HF-3c Level and on the CWS at DFT//HF-3c and DFT//DFT Level

Species		CWS		ASW									
		DFT//HF-3c	DFT//DFT	1	2	3	4	5	6	7	8	9	10
N	δE_S	−84	143	−96	168	36	−373	−397	289	−12	−24	…	…
	δE_μ	…	…	…	…	…	…	…	…	…	…	…	…
NH	δE_S	229	156	180	457	216	1034	−493	577	241	108	…	…
	δE_μ	12	−84	−12	24	−36	12	36	12	−12	12	…	…
NH_2	δE_S	409	481	−1058	674	529	662	168	156	758	325	…	…
	δE_μ	108	84	36	60	24	96	−12	36	108	24	…	…
NH_3	δE_S	738	451	1831	437	471	1916	750	988	591	…	…	…
	δE_μ	−329	−41	−124	−65	−84	−137	−7	22	−43	…	…	…
CN	δE_S	…	…	1600	361	649	1323	120	902	637	337	…	…
	δE_μ	…	…	−469	−325	−397	−337	−313	277	361	−469	…	…
HCN	δE_S	593	308	2355	1131	703	281	2368	1635	253	1629	…	…
	δE_μ	94	−795	216	114	−19	−83	53	−168	38	−168	…	…
HNC	δE_S	1127	853	2345	2021	2189	1768	−589	2430	2333	505	…	…
	δE_μ	671	494	698	541	589	830	758	625	613	421	…	…
N_2	δE_S	50	25	328	−54	65	74	−21	…	…	…	…	…
	δE_μ	−86	−65	−1	2	4	1	2	…	…	…	…	…
NO	δE_S	−36	60	−192	373	48	−24	457	24	…	…	…	…
	δE_μ	−84	12	96	−241	1	12	−132	−156	…	…	…	…
HNO	δE_S	337	253	565	1636	120	541	1612	1119	529	541	…	…
	δE_μ	144	72	73	84	36	132	144	96	24	−12	…	…
CH_3NH_2	δE_S	575	747	509	1082	649	361	373	1672	1143	830	…	…
	δE_μ	−12	35	−72	48	−24	60	−36	−23	12	−47	…	…
CH_3CN	δE_S	293	382	216	−1395	589	1539	433	−1058	926	192	…	…
	δE_μ	52	95	36	37	47	−253	96	35	49	…	…	…
OCN	δE_S	…	…	96	373	168	553	−253	926	120	119	…	…
	δE_μ	…	…	132	−180	−72	−60	108	36	−120	34	…	…
NH_2CN	δE_S	625	682	1203	1732	349	1960	241	445	1852	1335	541	1131

Table 7
(Continued)

Species		CWS		ASW									
		DFT//HF-3c	DFT//DFT	1	2	3	4	5	6	7	8	9	10
	δE_μ	36	250	−24	216	93	−156	204	108	−156	-108	120	13
HNCO	δE_S	553	806	1720	1828	1407	613	1335	2117	854	481	⋯	⋯
	δE_μ	565	349	−216	120	541	144	120	142	565	203	⋯	⋯
N_2O	δE_S	79	281	−21	1287	192	1070	119	601	710	192	⋯	⋯
	δE_μ	153	23	108	132	119	325	108	253	204	122	⋯	⋯
NH_2CHO	δE_S	1264	545	2769	937	1472	−719	1026	1044	3318	−1045	⋯	⋯
	δE_μ	−72	−478	91	99	65	98	−81	21	249	67	⋯	⋯
NO_2	δE_S	72	301	−120	36	96	842	−36	96	⋯	⋯	⋯	⋯
	δE_μ	−36	48	−49	−12	−25	−13	−25	59	⋯	⋯	⋯	⋯
HC_3N	δE_S	127	⋯	24	1034	842	229	385	854	457	216	⋯	⋯
	δE_μ	−14	⋯	36	144	229	37	−227	216	60	117	⋯	⋯
CH_2CHCN	δE_S	370	396	61	253	1696	2261	−1588	251	1828	1143	⋯	⋯
	δE_μ	85	38	36	71	−253	23	47	73	97	−49	⋯	⋯
HC_5N	δE_S	⋯	⋯	385	204	⋯	⋯	⋯	⋯	⋯	⋯	⋯	⋯
	δE_μ	⋯	⋯	168	96	⋯	⋯	⋯	⋯	⋯	⋯	⋯	⋯

Note. Units are in kelvins.

Appendix E
Hemibond Geometries for the CN Species

Figure 11 provides the adsorption geometries of the CN species on the ASW for the cases when a hemibond system is formed.

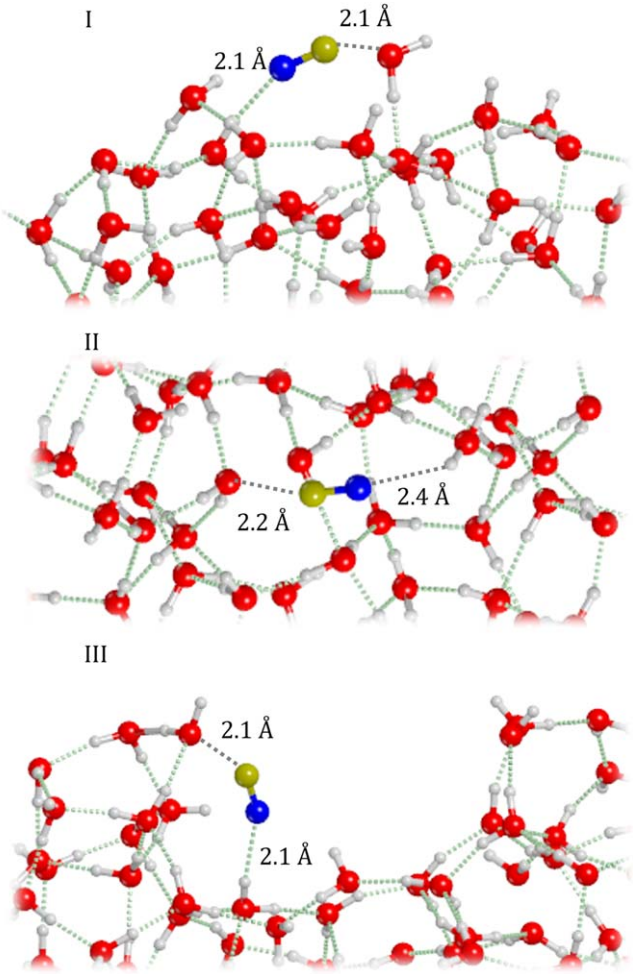

Figure 11. CN adsorption geometries for cases when a hemibond is formed. I for case 1; II for case 5; and III for case 6. Distances of H-bonds and hemibonds are included. Units are in Å.

Appendix F
Desorption Prefactors

Figure 12 provides the temperature dependence of the desorption rate prefactors computed for all the species in both models, the CWS and the ASW.

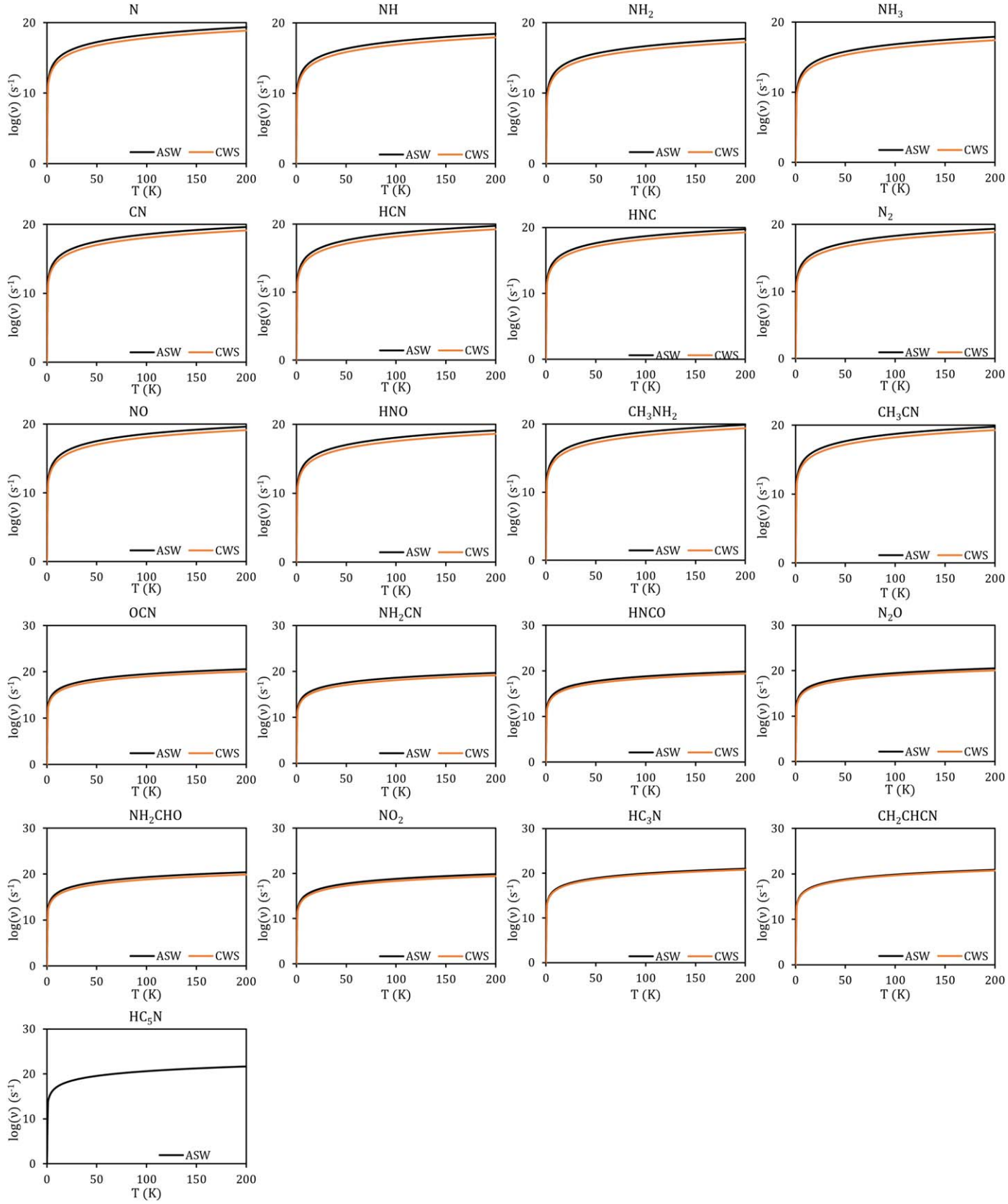

Figure 12. Temperature dependence of the desoprtion rate prefactors computed using Equation (5) (Tait et al. 2005). Black line correspond to the ASW model, and orange line to the CWS model. Parameters used computed the desorption rate prefactors temperature dependence are provided in Table 3.

ORCID iDs

Berta Martínez-Bachs https://orcid.org/0000-0002-1290-7019
Stefano Ferrero https://orcid.org/0000-0001-7819-7657
Cecilia Ceccarelli https://orcid.org/0000-0001-9664-6292
Piero Ugliengo https://orcid.org/0000-0001-8886-9832
Albert Rimola https://orcid.org/0000-0002-9637-4554

References

Al-Halabi, A., & Van Dishoeck, E. F. 2007, MNRAS, 382, 1648
Ásgeirsson, V., Jónsson, H., & Wikfeldt, K. T. 2017, J. Phys. Chem. C, 121, 1648
Becke, A. D. 1993, CP, 98, 1372
Boogert, A. A., Gerakines, P. A., & Whittet, D. C. 2015, ARA&A, 53, 541
Bovolenta, G., Bovino, S., Vöhringer-Martinez, E., et al. 2020, MolAs, 21, 100095
Bovolenta, G. M., Vogt-Geisse, S., Bovino, S., & Grassi, T. 2022, ApJS, 262, 17
Boys, S., & Bernardi, F. 1970, MolPh, 19, 553
Casassa, S., Ugliengo, P., & Pisani, C. 1997, CP, 106, 8030
Ceccarelli, C., Codella, C., Balucani, N., et al. 2023, in ASP Conf. Ser. 534, Protostars and Planets VII, ed. S. Inutsuka et al. (San Francisco, CA: ASP), 379
Ceccarelli, C. 2023, Faraday Discuss., 245, 11
Chaabouni, H., Diana, S., Nguyen, T., & Dulieu, F. 2018, A&A, 612, A47
Collings, M. P., Anderson, M. A., Chen, R., et al. 2004, MNRAS, 354, 1133
Cramer, C. J., & Bickelhaupt, F. 2003, Angew. Chem. Int. Ed., 42, 381
Cuppen, H., Walsh, C., Lamberts, T., et al. 2017, SSRv, 212, 1
Dapprich, S., Komáromi, I., Byun, K., Morokuma, K., & Frisch, M. J. 1999, JMoSt, 461-462, 1
Das, A., Sil, M., Gorai, P., Chakrabarti, S., & Loison, J. 2018, ApJS, 237, 9
Davidson, E. R., & Feller, D. 1986, ChRv, 86, 681
Dodson-Robinson, S. E., Willacy, K., Bodenheimer, P., Turner, N. J., & Beichman, C. A. 2009, Icar, 200, 672
Dohnálek, Z., Kimmel, G. A., Joyce, S. A., et al. 2001, JPhCB, 105, 3747
Douglas, A., & Herzberg, G. 1941, ApJ, 94, 381
Dovesi, R., Erba, A., Orlando, R., et al. 2018, Wiley Interdiscip. Rev. Comput. Mol. Sci., 8, e1360
Duflot, D., Toubin, C., & Monnerville, M. 2021, FrASS, 8, 645243
Dulieu, F., Congiul, F., Noble, J., et al. 2013, NatSR, 3, 2045
Dunham, T., Jr 1937, PASP, 49, 26
Dunning, T. H. 1989, CP, 90, 1007
Endres, C. P., Schlemmer, S., Schilke, P., Stutzki, J., & Müller, H. S. 2016, JMoSp, 327, 95
Fayolle, E. C., Balfe, J., Loomis, R., et al. 2016, ApJ, 816, L28
Ferrero, S., Grieco, F., Ibrahim Mohamed, A. S., et al. 2022, MNRAS, 516, 2586
Ferrero, S., Zamirri, L., Ceccarelli, C., et al. 2020, ApJ, 904, 11
Frisch, M. J., Trucks, G. W., Schlegel, H. B., et al. 2016, Gaussian16 Revision C.01 (Wallingford, CT: Gaussian Inc.)
Germain, A., Tinacci, L., Pantaleone, S., Ceccarelli, C., & Ugliengo, P. 2022, ACS Earth Space Chem., 6, 1286
Grimme, S., Ehrlich, S., & Goerigk, L. 2011, JCoCh, 32, 1456
Hartmann, L., Ciesla, F., Gressel, O., & Alexander, R. 2017, SSRv, 212, 813
He, J., Acharyya, K., & Vidali, G. 2016, ApJ, 825, 89
Hendrix, J., Bera, P. P., Lee, T. J, & Head-Gordon, M 2023, MolPh, 122, e2252100
Jansen, H., & Ros, P. 1969, CPL, 3, 140
Karssemeijer, L. J., & Cuppen, H. M. 2014, A&A, 569, A107
Karssemeijer, L. J., de Wijs, G. A., & Cuppen, H. M. 2014, Phys. Chem. Chem. Phys., 16, 15630
Kolasinski, K. W. 2012, Surface Science: Foundations of Catalysis and Nanoscience (New York: John Wiley & Sons),
Lee, C., Yang, W., & Parr, R. G. 1988, PhRvB, 37, 785
Liu, B., & McLean, A. 1973, JChPh, 59, 4557
López-Sepulcre, A., Balucani, N., Ceccarelli, C., et al. 2019, ESC, 3, 2122
McClure, M. K., Rocha, W. R. M., Pontoppidan, K. M., et al. 2023, NatAs, 7, 431
McGuire, B. A. 2022, ApJS, 259, 30
McKellar, A. 1940, PASP, 52, 187
Minissale, M., Aikawa, Y., Bergin, E., et al. 2022, ESC, 6, 597
Mollière, P., Molyarova, T., Bitsch, B., et al. 2022, ApJ, 934, 74
Noble, J. A., Congiu, E., Dulieu, F., & Fraser, H. J. 2012, MNRAS, 421, 768
Oba, Y., Miyauchi, N., Hidaka, H., et al. 2009, ApJ, 701, 464
Öberg, K. I., & Bergin, E. A. 2021, PhR, 893, 1
Öberg, K. I., Murray-Clay, R., & Bergin, E. A. 2011, ApJL, 743, L16
Öberg, K. I., & Wordsworth, R. 2019, AJ, 158, 194
Oró, J. 1960, BBRC, 2, 407
Papajak, E., Zheng, J., Xu, X., Leverentz, H. R., & Truhlar, D. G. 2011, J. Chem. Theory Comput., 7, 3027
Pascale, F., Zicovich-Wilson, C. M., López Gejo, F., et al. 2004, J. Comput. Chem., 25, 888
Penteado, E., Walsh, C., & Cuppen, H. 2017, ApJ, 844, 71
Perdew, J. P., Burke, K., & Ernzerhof, M. 1996, PhRvL, 77, 3865
Perrero, J., Enrique-Romero, J., Ferrero, S., et al. 2022, ApJ, 938, 158
Pisani, C., Casassa, S., & Ugliengo, P. 1996, CPL, 253, 201
Pople, J. A., Gill, P. M. W., & Handy, N. C. 1995, IJQC, 56, 303
Rimola, A., Skouteris, D., Balucani, N., et al. 2018, ESC, 2, 720
Saitta, A. M., & Saija, F. 2014, PNAS, 111, 13768
Saladino, R., Botta, G., Pino, S., Costanzo, G., & Di Mauro, E. 2012a, Chem. Soc. Rev., 41, 5526
Saladino, R., Crestini, C., Pino, S., Costanzo, G., & Di Mauro, E. 2012b, Phys. Life Rev., 9, 84
Sameera, W., Senevirathne, B., Andersson, S., Maseras, F., & Nyman, G. 2017, J. Phys. Chem. C, 121, 15223
Santalucia, R., Pazzi, M., Bonino, F., et al. 2022, PCCP, 24, 7224
Schäfer, A., Horn, H., & Ahlrichs, R. 1992, CP, 97, 2571
Senevirathne, B., Andersson, S., Dulieu, F., & Nyman, G. 2017, MolAs, 6, 59
Shimonishi, T., Nakatani, N., Furuya, K., & Hama, T. 2018, AJ, 855, 27
Smith, R. S., May, R. A., & Kay, B. D. 2016, JPCB, 120, 1979
Sure, R., & Grimme, S. 2013, JCoCh, 34, 1672
Swings, P., & Rosenfeld, L. 1937, ApJ, 86, 483
Tait, S. L., Dohnálek, Z., Campbell, C. T., & Kay, B. D. 2005, CP, 122, 164708
Tinacci, L., Germain, A., Pantaleone, S., et al. 2023, ApJ, 951, 32
Tatewaki, H., & Huzinaga, S. 1980, JCoCh, 1, 205
Tinacci, L., Germain, A., Pantaleone, S., et al. 2022, ESC, 6, 1514
Tóth Ugyonka, H., Hantal, G., Szőri, M., & Jedlovszky, P. 2024, ESC, 8, 520
Ugliengo, P., Viterbo, D., & Chiari, G. 1993, Z. Kristallogr. Cryst. Mater., 207, 9
Wakelam, V., Loison, J., Mereau, R., & Ruaud, M. 2017, MolAs, 6, 22
Watanabe, N., & Kouchi, A. 2008, PrSS, 83, 439
Zamirri, L., Casassa, S., Rimola, A., et al. 2018, MNRAS, 480, 1427
Zamirri, L., Corno, M., Rimola, A., & Ugliengo, P. 2017, ESC, 1, 384
Zamirri, L., Pantaleone, S., & Ugliengo, P. 2019, JChPh, 150, 064702
Zicovich-Wilson, C. M., Pascale, F., Roetti, C., et al. 2004, JCoCh, 25, 1873